

A ¹¹⁵In Solid-State NMR Study of Low Oxidation-State Indium Complexes

Hiyam Hamaed,¹ Karen E. Johnston,¹ Benjamin F. T. Cooper,¹ Victor V. Terskikh,² Eric Ye,³
Charles L. B. Macdonald,¹ Donna C. Arnold,⁴ and Robert W. Schurko^{1,*}

¹Department of Chemistry and Biochemistry, University of Windsor, Windsor, Ontario, Canada,
N9B 3P4

²Steacie Institute for Molecular Sciences, National Research Council Canada, Ottawa, Ontario,
Canada, K1A 0R6

³Department of Chemistry, University of Ottawa, Ottawa,
Ontario, Canada, K1N 6N5

⁴School of Physical Sciences, University of Kent, Canterbury, Kent, United Kingdom, CT2 7NH

*Author to whom correspondence should be addressed

Phone: (519) 253-3000 x3548, Fax: (519) 973-7098

Electronic mail: rschurko@uwindsor.ca

Abstract

^{115}In solid-state NMR (SSNMR) spectroscopy is applied to characterise a variety of low oxidation-state indium(I) compounds. ^{115}In static wideline SSNMR spectra of several In(I) complexes were acquired with moderate and ultra-high field NMR spectrometers (9.4 and 21.1 T, respectively). ^{115}In MAS NMR spectra were obtained with moderate and ultra-fast (> 60 kHz) spinning speeds at 21.1 T. In certain cases, variable-temperature (VT) ^{115}In SSNMR experiments were performed to study dynamic behaviour and phase transitions. The indium electric field gradient (EFG) and chemical shift (CS) tensor parameters were determined from the experimental spectra. With the aid of first principles calculations, the tensor parameters and orientations are correlated to the structure and symmetry of the local indium environments. In addition, calculations aid in proposing structural models for samples where single crystal X-ray structures could not be obtained. The rapidity with which high quality ^{115}In SSNMR spectra can be acquired at 21.1 T and the sensitivity of the ^{115}In NMR parameters to the indium environment suggest that ^{115}In SSNMR is a powerful probe of the local chemical environments of indium sites. This work demonstrates that ^{115}In NMR can be applied to a wide range of important materials for the purpose of increasing our understanding of structures and dynamics at the molecular/atomic level, especially for the characterisation of disordered, microcrystalline and/or multi-valence solids for which crystal structures are unavailable.

Keywords: solid-state NMR spectroscopy; ^{115}In NMR; WURST-echo pulse sequence; quadrupolar nuclei; ab initio calculations; low-oxidation state;

Introduction

There is increasing interest in exploring new compounds with metal elements in low oxidation-states for the synthesis of catalysts or materials precursors.¹⁻⁶ Compounds with metal elements in lower oxidation states have very different structural features and reactivities than corresponding higher oxidation state compounds.^{7,8} For the lighter group 13 elements, the +3 oxidation state is usually the most stable and compounds containing such centres typically behave as Lewis acids. With the exception of thallium, compounds containing group 13 elements in the +1 oxidation state are comparatively rare and have the capacity to act either as Lewis bases or Lewis acids or both.^{9,10} Indium, which sits between the lighter group 13 elements and thallium, is somewhat unique in that the relative stabilities of the +3 and +1 oxidation states are similar. Although the trivalent state is generally more stable, there are numerous examples of relatively stable univalent indium compounds.¹¹ Investigation of indium species can provide insight into what factors affect the redox stability and chemistry of group 13 and other *p*-block compounds. In addition to the fundamental chemical insights that may be obtained from the study of such species, In(I) compounds also exhibit unique behavior and redox properties which make them useful as either reagents or catalysts employed to effect several types of organic transformations.^{6,11-16} Finally, it should be noted that the majority of inorganic In(I) salts are insoluble (or unstable) in most common organic solvents,^{7,17} which limits their structural characterisation by routine methods (i.e., single crystal X-ray diffraction and solution NMR). This also means that the reactions in which they are used are often heterogeneous in nature. Recently, crown ethers have been proven to be useful ligands for the stabilisation and increased solubilisation of some indium(I) reagents.^{10,13,18}

Indium has two NMR-active isotopes, ^{113}In and ^{115}In , which are quadrupolar nuclei (both have nuclear spins of $9/2$). They both have large nuclear electric quadrupole moments ($Q = 75.9$ and 77.0 fm^2 , respectively),^{19,20} moderate gyromagnetic ratios (5.8845×10^7 and $5.8972 \times 10^7 \text{ rad T}^{-1} \text{ s}^{-1}$, respectively) and natural abundances of 4.3 % and 95.7 %, respectively.²¹ Of the two isotopes, ^{115}In is preferred for NMR due to its much higher receptivity (i.e., with respect to carbon, $D^{\text{C}}(^{113}\text{In}) = 88.5$ and $D^{\text{C}}(^{115}\text{In}) = 1.98 \times 10^3$); however, its quadrupole moment is the largest among all NMR-active isotopes of the main group elements. The large Q can lead to sizeable quadrupolar interactions, resulting in very broad NMR patterns which are challenging to acquire.²² The quadrupolar interaction is the interaction of the nuclear quadrupole moment with the electric field gradient (EFG) at the nucleus. The EFG is described by a symmetric, traceless, second-rank (3×3) tensor with three principal components defined such that $|V_{33}| \geq |V_{22}| \geq |V_{11}|$. These components provide information about the spherical and axial symmetry of the ground state electronic environment at the nuclear site via measurements of the quadrupolar coupling constant, $C_Q = eQV_{33}/h$, and the asymmetry parameter, $\eta_Q = (V_{11} - V_{22})/V_{33}$, respectively. Measurements of the ^{115}In EFG tensor components, along with the indium chemical shift (CS) tensor parameters (which describe the indium chemical shift anisotropy, CSA) provide useful information about the chemical environments of the indium atoms.

Solution-state ^{115}In NMR spectroscopy has been used to identify different indium sites in a variety of In(III)-containing systems through measurements of the isotropic chemical shifts, δ_{iso} .²³⁻³² However, in cases where indium sites are not in spherically symmetric environments, it is often difficult to observe the ^{115}In NMR signal, due to fast quadrupolar relaxation in solution.²⁶ Furthermore, many In(I) compounds are insoluble or unstable in commonly used solvents, limiting the application of solution-state NMR spectroscopy for their study.^{11,17} ^{115}In solid-state

NMR (SSNMR) is an excellent option for characterisation of such systems, since the anisotropic NMR interaction tensors obtained from these spectra provide rich structural information. Most of the ^{115}In SSNMR studies reported to date have largely focused on indium materials which are used (or have the potential to be used) as semi-conductors or conductors.³³⁻⁴⁰ Many of these studies report indium Knight shifts, sometimes the quadrupolar parameters, and rarely, the chemical shift (CS) tensor parameters. In addition, most of these studies deal with indium materials in which In is in the +3 oxidation state and/or exists in highly symmetric environments. Recently, Chen *et al.* have shown the utility of ^{115}In SSNMR for studying indium coordination complexes in which the indium is in the +3 oxidation state,^{22,41} and Bryce and coworkers have reported ^{115}In ultra-wideline NMR spectra of two In(I)bis(imino)pyridine analogues.⁴²

Herein, we describe the first detailed ^{115}In SSNMR study of low oxidation-state indium compounds. ^{115}In SSNMR data are obtained for eight samples with a variety of structural motifs, including $[\text{In}][\text{GaCl}_4]$, InBr , InI , $[\text{In}][\text{OTf}]$ (OTf = trifluoromethanesulfonate), $[\text{In}([15]\text{crown-5})_2][\text{OTf}]$, $[\text{In}([18]\text{crown-6})][\text{OTf}]$, $[\text{In}([18]\text{crown-6})][\text{GaCl}_4]$ and $[\text{In}([18]\text{crown-6})][\text{AlCl}_4]$. Static (i.e., stationary sample) NMR spectra were acquired at both moderate and ultra-high magnetic field strengths (9.4 and 21.1 T) in order to accurately measure the EFG and CS tensor parameters. In addition, magic-angle spinning (MAS) spectra were obtained at 21.1 T in order to average the contribution of the indium CSA to the central transition (CT, $+1/2 \leftrightarrow -1/2$) pattern, and to separate the central isotropic powder pattern from the spinning sidebands, thereby allowing for accurate measurements of C_Q , η_Q and δ_{iso} . In most cases, the use of ultra-fast ($v_{\text{rot}} = 50$ kHz) MAS was necessary, due to the sizeable anisotropic NMR interactions. There are very few reports of ^{115}In MAS NMR in the literature;^{35,38,43,44} to the best of our knowledge, this is the first report of ^{115}In MAS NMR spectra acquired under ultra-fast MAS conditions. Analytical

simulations of the ^{115}In static NMR spectra are used to determine the quadrupolar and CS parameters, which are correlated to the local structure and symmetry at the indium sites. Variable-temperature (VT) powder X-ray diffraction (pXRD) and ^{115}In NMR experiments were performed on $[\text{In}([15]\text{crown-5})_2][\text{OTf}]$ to study its phase transitions and temperature-dependent molecular dynamics. Finally, first principles calculations of the indium EFG and nuclear magnetic shielding (NS) tensors are presented for systems for which structures are available, using plane-wave density functional theory (DFT) methods in the CASTEP software package.⁴⁵ These calculations, in combination with NMR and pXRD experiments, also aid in proposing structural models for systems for which single crystal structures cannot be obtained.

Experimental Details

Sample Preparation. Samples of InBr and InI were purchased from Sigma-Aldrich and used without purification. [In][GaCl₄], [In][OTf], [In([15]crown-5)₂][OTf], [In([18]crown-6)][OTf], [In([18]crown-6)][AlCl₄] and [In([18]crown-6)][GaCl₄] were synthesised as described in the literature.^{13,46}

X-ray Diffraction. Powder X-ray diffraction (pXRD) experiments were carried out at room temperature and 45 °C on a Bruker AXS HI-STAR system by using a general area detector diffractions system and Cu K_α ($\lambda = 1.540598 \text{ \AA}$) radiation. Diffraction data were analysed by Rietveld and LeBail refinement using the General Structure Analysis System (GSAS) software package.⁴⁷ Parameters refined included background coefficients, detector zero point, instrumental parameters, lattice parameters and profile coefficients. Diffraction data were also analysed using the Chekcell software⁴⁸ and the Crysfire suite of programs using the indexing program Dicvol.⁴⁹⁻⁵¹

Solid-State NMR Spectroscopy. ¹¹⁵In SSNMR experiments were performed on a Varian InfinityPlus spectrometer equipped with a 9.4 T ($\nu_0(^1\text{H}) = 399.73 \text{ MHz}$) Oxford wide-bore magnet ($\nu_0(^{115}\text{In}) = 87.59 \text{ MHz}$) at the University of Windsor and a 21.1 T ($\nu_0(^1\text{H}) = 900.08 \text{ MHz}$) Bruker Avance II spectrometer ($\nu_0(^{115}\text{In}) = 197.23 \text{ MHz}$) at the National Ultrahigh-Field NMR Facility for Solids in Ottawa, Canada. In some cases, the NMR patterns are much broader than the excitation bandwidths achievable with an ideal high-power rectangular pulse; thus, spectra were collected by stepping the transmitter frequency across the entire CT powder pattern in even increments, acquiring the individual sub-spectra, and co-adding them to form the total pattern^{52,53} (see Supporting Information, Tables S1-S3 for full experimental details). For [In([15]crown-5)₂][OTf], spectra were obtained at room temperature as well as at 45 °C. Indium

chemical shifts were referenced to 0.1 M solution of $\text{In}(\text{NO}_3)_3$ in 0.5 M HNO_3 ($\delta_{\text{iso}} = 0.0$ ppm).²² Analytical simulations of ^{115}In NMR spectra were performed using WSolids, and MAS NMR spectra with spinning sidebands simulated using DMFit.⁵⁴

Experiments at 9.4 T. Samples were finely ground and packed into either 5 mm o.d. zirconium oxide rotors or 5 mm o.d. glass NMR tubes. ^{115}In static NMR spectra were acquired using a Varian 5 mm triple-resonance MAS probe (HXY). Spectra were collected at room temperature using either a Hahn-echo sequence of the form $(\pi/2)_x-\tau_1-(\pi)_y-\tau_2$ -acq (where τ_1 and τ_2 represent interpulse delays), or the WURST-echo pulse sequence.⁵⁵ For the Hahn-echo experiments, CT selective $\pi/2$ pulse widths between 0.45 μs ($\nu_1 = 111$ kHz) and 1.1 μs ($\nu_1 = 45$ kHz), an optimised recycle delay of 0.1 s and a spectral width of 1 or 2 MHz were used. The transmitter offset frequency was set between 35 and 150 kHz. For the WURST-echo experiments, WURST-80 pulse shapes⁵⁶ were used with a 50 μs WURST pulse length, and swept at a rate of 40 MHz/ms with an offset of 1000 kHz and rf power of 17 kHz. A spectral width of 2 MHz and recycle delay of 0.1 s were used. The frequency step size was set to 250 kHz, in order to ensure uniform excitation. Spectra were also acquired at 45 °C for $[\text{In}([\text{15}]\text{crown-5})_2][\text{OTf}]$, utilizing a Bloch-decay sequence with a CT selective $\pi/2$ pulse width 0.5 μs , an optimised recycle delay of 0.1 s, ^1H decoupling power of 48 kHz and a spectral width of 2 MHz. Further experimental details are given in Table S1.

Experiments at 21.1 T. For the static ^{115}In NMR experiments, samples were ground and packed into 4 mm o.d. NMR glass tubes and spectra were acquired on a 4 mm home-built static (HX) probe using a solid-echo pulse sequence of the form $(\pi/2)_x-\tau_1-(\pi/2)_y-\tau_2$ -acq. Experiments were conducted with a selective $\pi/2$ pulse width of 0.5 μs ($\nu_1 = 100$ kHz) or 1 μs ($\nu_1 = 50$ kHz), spectral widths between 200 and 2000 kHz, a recycle delay of 1 s. In cases where piecewise

acquisition was necessary, the transmitter frequency offsets were set between 60 and 150 kHz. A ^1H decoupling power of 55 kHz was applied for the spectral acquisitions of proton-containing samples; however, decoupling did not seem to alter the shape of the powder patterns. In the case of $[\text{In}([\text{15}]\text{crown-5})_2][\text{OTf}]$, spectra were also acquired at 45 °C with a Bloch decay sequence. Further experimental details are given in Table S2.

MAS NMR spectra were acquired using either 4 mm or 1.3 mm Bruker double-resonance probes, using the solid-echo pulse sequence with rotor-synchronised echo delays for all samples, with the exception of $[\text{In}([\text{15}]\text{crown-5})_2][\text{OTf}]$, for which the Bloch decay sequence was used. Selective $\pi/2$ pulse widths of 0.5 ($\nu_1 = 100$ kHz) or 1 μs ($\nu_1 = 50$ kHz), spectral widths between 200 and 1000 kHz, recycle delays of either 0.5 or 1 s were used, with spinning speeds from 12.5 to 62.5 kHz (Table S3).

In variable temperature NMR experiments at 21.1 T the sample temperature was controlled by a Bruker BVT 3000 digital temperature controller coupled with a BCU05 cooling unit. Under MAS conditions the actual sample temperature was calibrated using a ^{79}Br NMR signal in spinning KBr according to reference 57. All reported temperatures are accurate with plus minus 2 °C.

Computational Methods. ^{115}In EFG and NS tensor parameters were calculated for all systems with available crystal structures.^{13,46,58-60} We distinguish theoretically derived nuclear shielding (NS) and experimentally measured chemical shift (CS) tensor parameters; the former are converted to the CS scale for comparison, as described in Table 2. For systems without known structures, the NMR interaction tensors were calculated for model systems, and used to propose potential structures. Plane-wave DFT calculations were performed using the CASTEP DFT code⁴⁵ in the Materials Studio 5.0 software suite on a Dell Studio XPS 9100 desktop with

an Intel(R) Core(TM) i7 at 2.67 GHz processor and 8 GB DDR3 RAM. CASTEP is a plane-wave pseudopotential method that utilises the gauge-including projector-augmented wave (GIPAW) formalism.⁶¹ The generalized gradient approximation (GGA) and revised Perdew, Burke and Ernzerhof (rPBE) functional were used, with the core valence interactions being described by on-the-fly pseudopotentials.^{62,63} Integrals over the Brillouin zone were performed using a Monkhorst-Pack grid with a k-point spacing of 0.08 \AA^{-1} . Wavefunctions were expanded in plane waves, with kinetic energy less than a cut-off energy, typically 360 or 610 eV.

Results and Discussion

Solid-State ^{115}In NMR

In this section, the ^{115}In SSNMR data are discussed for the eight samples. The EFG and CS tensor parameters are summarised in Table 1. We note that the MAS NMR spectra were only obtained at 21.1 T; since the breadths of CT NMR spectra are inversely proportional to the applied magnetic field strength, it is possible to separate the spinning sidebands from the isotropic powder pattern, and accurately determine C_Q , η_Q and δ_{iso} .

In all cases the isotropic chemical shifts are consistent with the indium atoms being in the +1 oxidation state, since the measured chemical shifts indicate that nuclei of the In(I) sites are much more shielded than those reported for In(III) complexes in solution and in the solid state,^{22,30,41} consistent with chemical shifts of In(I) sites measured with solution ^{115}In NMR spectroscopy.^{18,28,64,65}

Indium Tetrachlorogallate, $[\text{In}][\text{GaCl}_4]$

The ^{115}In SSNMR spectra of $[\text{In}][\text{GaCl}_4]$ (Figure 1(a)) reveal a single indium site, in agreement with the crystal structure.⁵⁹ The indium site in this structure is coordinated by six chlorine atoms in a distorted octahedral environment (Scheme 1(a)). The C_Q value (Table 1) is small in comparison to the larger C_Q values of the six-coordinate indium(III) complexes reported by Chen *et al.*^{22,41} and the indium(I) complexes studied by Bryce *et al.*⁴² However, it is similar to that of $\text{Na}_3\text{In}^{\text{III}}\text{Cl}_6$ ($C_Q = 20.11$ MHz), in which the indium atom is also in a distorted octahedral environment. The non-zero η_Q value indicates the absence of a threefold (or higher) rotational symmetry axis, and that the largest component of the EFG tensor, V_{33} , is distinct. The terminology *distinct* is used herein to denote the principal component of an NMR interaction

tensor which is furthest in absolute magnitude from the other two components (e.g., if $\eta_Q = 0.1$, then V_{33} is distinct, and V_{11} and V_{22} are similar in magnitude). In cases of perfect axial symmetry, $\eta_Q = 0$, or absence of an EFG component in one direction, $\eta_Q = 1$, the terminology *unique* is utilised (i.e., if $\eta_Q = 0$, then V_{33} is unique and $|V_{11}| = |V_{22}|$; if $\eta_Q = 1$, then V_{11} is unique, and $|V_{33}| = |V_{22}|$). The only symmetry element present is a mirror plane, and hence, V_{33} must be oriented within or perpendicular to this mirror plane; however, no further comment can be made on its actual orientation, and this is left to the discussion in the computational section below. Despite the fact that the powder pattern of $[\text{In}][\text{GaCl}_4]$ is dominated by the quadrupolar interaction, the CSA contribution has a major effect on its shape, as clearly seen from the static spectrum acquired at 21.1 T (Figure S1). The Euler angle β is close to zero, indicating that V_{33} and the principal component of the NS tensor corresponding to the direction of the highest shielding, σ_{33} , are almost coincident.

Indium(I) Iodide, InI and Indium(I) Bromide, InBr

The structures of InI and InBr are isomorphous, each having seven halogen atoms in the first coordination sphere of In.⁶⁶ The coordination geometry around the indium is described as a “7-octahedron”⁶⁰ or capped trigonal prismatic (Scheme 1(b), 1(c)). Simulations of the NMR spectra (Figure 2) reveal a single indium site in each case, in agreement with the structures.^{58,60} The relatively large C_Q values result in broad NMR patterns which necessitate the use of an ultra-fast spinning speed (62.5 kHz) and $B_0 = 21.1$ T in order to obtain the MAS NMR spectra. In the static spectra acquired at 9.4 T, lower intensity powder patterns associated with the STs clearly overlap with the CT patterns. Interestingly, spinning sidebands (SSBs) arising from STs are visible in the MAS NMR spectra acquired at 21.1 T, extending well beyond the range of

SSBs associated with the CT; however STs are not clearly visible in the static NMR spectra acquired at this field. The C_Q of InBr is higher than that of InI, possibly due to the difference in electronegativity between Br and I. C_Q values of metal nuclides have been observed to increase (in absolute magnitude) with the increasing electronegativity of the halide atoms in the first coordination sphere in isostructural BiOX (X = Cl, Br, I) systems,⁶⁷ as well as in GaX,⁶⁸ AsX₃,^{69,70} SbX₃⁷¹⁻⁷³ and (NbX₅)_y (y = 2 or 4).^{74,75} The indium CSA contributions are small in both cases; however, the inclusion of the CS tensor parameters is again necessary in order to achieve the best fits (Figures S2 and S3). Finally, the low values of β indicate that V_{33} and σ_{33} are almost coincident in both systems.

Indium(I) Trifluoromethanesulfonate, [In][OTf]

The structure of [In][OTf] has two indium sites with very similar geometries.⁴⁶ The coordination environments of the indium atoms consist of four short contacts (less than 3 Å) with oxygen atoms of different triflate anions, and eight other oxygen and fluorine contacts within 4 Å (Scheme 1(d)). The four short contacts are arranged in an approximately “see-saw” geometry⁴⁶ and are oriented to one side of each indium atom. The ¹¹⁵In NMR patterns (Figure 3) are very broad compared to the other simple In(I) salts (i.e., 575 kHz at 9.4 T and 290 kHz at 21.1 T) discussed thus far. Once again, there is some evidence of ST patterns in the static and MAS spectra acquired at 9.4 T and 21.1 T, respectively. Due to the structural similarities of the two sites, the NMR parameters are very similar, and the spectra acquired at 21.1 T do not aid in differentiating the two sites. Surprisingly, there is some evidence of the two separate sites in the static ¹¹⁵In NMR spectrum acquired at 9.4 T, though the mediocre S/N prevents the accurate measurement of the splittings. Structurally similar sites are most often distinguished via slight

differences in values of δ_{iso} , which are more easily differentiated at higher magnetic fields due to the higher frequency dispersion of chemical shifts. In this case, it is very likely that the values of δ_{iso} for the two In(I) sites are identical (or very close), and therefore not resolved at either field. However, the C_Q (and possibly η_Q) values are different enough that two patterns can be partially resolved at 9.4 T, since the effect of the second-order quadrupolar interaction on the CT pattern breadth scales as the inverse of B_0 . Unfortunately, we were not able to obtain reliable parameters from a two site fit, and therefore only report one set of parameters with larger uncertainties (a two site fit of the 9.4 T spectrum is possible, but the parameters for each site are within the other site's experimental uncertainties, Figure S4). The C_Q value of this sample is larger than those discussed above, which is likely due to the spherically asymmetric environment about the In centre arising from the stereochemically active lone pair of the indium atom. The almost zero η_Q value indicates that the EFG tensor is nearly axially symmetric and that V_{33} is the distinct component. The span is also large, but contributes only to ca. 9% of the total breadth of the NMR pattern (Figure S5).

Indium(I)[15]crown-5-Sandwich Trifluoromethanesulfonate, [In([15]crown-5)₂][OTf]

This was the first structurally-characterised complex of indium and [15]crown-5; in addition, it is unusually soluble in toluene.¹³ The structure has a single indium site residing on an inversion centre (Scheme 1(e)). The ¹¹⁵In NMR spectra reveal the presence of a single indium site with a relatively small C_Q (Figure 4), which is consistent with its highly spherically symmetric environment. The small non-zero η_Q again confirms the absence of a threefold (or higher) rotational axis and is consistent with the presence of an inversion centre. The indium CSA also makes a significant contribution to the powder pattern (Figure S6), with the Euler

angle of $\beta = 90^\circ$ revealing that σ_{33} is oriented in a direction perpendicular to V_{33} . However, the skew and other Euler angles do not indicate the coalignment of σ_{11} or σ_{22} with V_{33} . This compound also has some temperature-dependent structural changes which can be monitored with ^{115}In SSNMR; this is discussed later in this work.

Indium(I)[18]crown-6-Trifluoromethanesulfonate, [In([18]crown-6)][OTf]

This compound was the first structurally-characterised example of a coordination complex in which a monomeric In^{I} ion behaved as a Lewis acid.¹⁰ The crystal structure exhibits a single indium site positioned on the centroid of the O_6 ring (Scheme 1(f)). The ^{115}In NMR spectrum of this sample is much broader than those of the other systems discussed herein, and is not strongly influenced by even a large indium CSA; therefore, we report only the spectrum at 21.1 T acquired under static conditions (Figure 5). The simulation reveals a single indium site in agreement with the crystal structure. The C_Q value of this site is much larger in comparison to those of the other systems, due to both the reduced spherical symmetry at the indium site which results from the stereochemically active lone pair of the indium atom (as in the case of $[\text{In}][\text{OTf}]$), the interaction of the indium atom with only one crown (as opposed to the case of the [15]crown-5 sandwich compound), and the much closer interaction of the indium atom with a single oxygen atom from the proximate triflate group. The η_Q value indicates an axially symmetric ^{115}In EFG tensor, suggesting the largest component of the tensor, V_{33} , is colinear with the pseudo-rotational axis (*vide infra*).

Indium(I)-[18]crown-6-gallium tetrachloride and Indium(I)-[18]crown-6-aluminium tetrachloride, [In([18]crown-6)][GaCl₄] and [In([18]crown-6)][AlCl₄]

The structures of these compounds have not been obtained due to the difficulties in growing crystals suitable for single crystal XRD experiments. Powder XRD experiments were completed and the corresponding diffraction patterns are shown in Figure S7. Therefore, ¹¹⁵In SSNMR is an ideal tool for providing insights into the electronic and bonding environments of the indium sites, and the arrangement of the different ligands. The static CT patterns are narrower than those of [In([18]crown-6)][OTf], hence, spectra were acquired at both 9.4 and 21.1 T, in order to aid in elucidating the indium CS tensor parameters and to refine the EFG tensor parameters. Due to the broad patterns, ¹¹⁵In static NMR spectra (Figure 6) were acquired at 9.4 T using frequency-stepped techniques (i.e., the variable-offset cumulative spectra method).^{52,53} At 21.1 T it was possible to acquire MAS spectra using an ultra-fast MAS NMR probe ($\nu_{\text{rot}} = 50$ kHz), as well as static spectra in a single experiment (i.e., there is no need to use frequency-stepped acquisitions, Figure 6).

Simulations of the spectra reveal a single indium site in each of [In([18]crown-6)][GaCl₄] and [In([18]crown-6)][AlCl₄] with similar NMR parameters, indicating that these sites exist in similar chemical environments. The C_Q values indicate In environments of considerably lower spherical symmetry than that of [In([15]crown-5)₂][OTf]. The indium CSA has some effects on the static CT powder patterns at 21.1 T which could not be accurately simulated without the inclusion of the CS tensor parameters (Figure S8). The ¹¹⁵In NMR parameters obtained from simulations suggest that these In environments, and the overall molecular structures, must be very different from those of [In([15]crown-5)₂][OTf] and [In([18]crown-6)][OTf]. Their stoichiometry and quadrupolar parameters suggest that there is only a single crown ether

interacting with each indium site; however, the C_Q is much smaller than that of [In([18]crown-6)][OTf], implying that structural arrangements similar to this are unlikely. Given that the [18]crown-6 cavity is large enough to accommodate the In(I) ion,⁷⁶ and given that interactions between the tetrachloride ions and indium are a possibility (and would certainly result in a reduced C_Q compared to [In([18]crown-6)][OTf]), we propose the structural model pictured in Scheme 1(g). The presence of GaCl₄ and AlCl₄ are confirmed by ⁷¹Ga and ²⁷Al SSNMR spectra (Figure S9), based on their solution chemical shifts.³⁰ However, further ¹¹⁵In NMR experiments should be performed on similar well-characterised systems which, in combination with first principles calculations, can be utilised to confirm the proposed structures.

Variable Temperature SSNMR and pXRD Experiments on [In([15]crown-5)₂][OTf].

While conducting ¹¹⁵In NMR experiments on [In([15]crown-5)₂][OTf] under conditions of MAS ($v_{\text{rot}} = 18$ kHz), some unexpected changes in spectral appearance were noted. Since spinning the sample causes frictional heating (ca. +22 °C above room temperature at 18 kHz on our Bruker 4 mm HX probe), we postulated that the spectra were indicating some sort of temperature-dependent behaviour, possibly including dynamic exchange and/or a solid-solid phase transition. A differential scanning calorimeter (DSC) experiment was performed, with results indicating that a phase transition occurs at ca. 42 °C (data not shown). This phase transition was found to be reversible, as the sample reconverts back to the original solid phase when cooled back down to room temperature.

Variable-temperature (VT) NMR and pXRD experiments have been performed to understand the structural differences between the two phases and characterise the new higher-temperature form. VT ¹³C and ¹H MAS NMR spectra reveal that the carbon and proton chemical shifts are very similar in both forms (Figure S10, S11). However, VT ¹¹⁵In SSNMR experiments

conducted at 21 and 45 °C show that the two different forms have distinct ^{115}In NMR patterns (Figure 7). The featureless Gaussian NMR lineshape of the 45 °C form is likely due to dynamic positional disorder of the indium site, and not to an amorphous phase, since pXRD experiments indicate that the sample is crystalline at this temperature (*vide infra*). Exact values of C_Q and η_Q cannot be determined for the 45 °C pattern, since there are no visible discontinuities. However, using the QuadFit software package,⁷⁷ we are able to estimate a range of C_Q values from 17 to 21 MHz, and a range of η_Q values from 0.85 to 1. The distinct spectral line widths of the 45 °C sample at two different magnetic field strengths signify that the broadening arises from a distribution of field-dependent NMR interactions, and not purely T_2 broadening. In fact, since the 45 °C pattern is ca. half of the breadth of the 21 °C pattern, and given that second-order quadrupolar broadening of the CT scales as the inverse of the applied magnetic field, it is very likely that these patterns are dominated by the second-order quadrupolar interaction. Unfortunately, due to the lack of defining discontinuities in this pattern, we are unable to quantify the nature of the dynamical averaging of the EFG tensors.

Refinement of the room temperature powder X-ray diffraction pattern collected for $[\text{In}([\text{15}]\text{crown-5})_2][\text{OTf}]$ clearly indicates a single phase and displays excellent agreement with the triclinic P-1 model reported by Cooper *et al.* (Figure 9).¹³ The pXRD pattern obtained for the high temperature form of $[\text{In}([\text{15}]\text{crown-5})_2][\text{OTf}]$ exhibits fewer peaks when compared to the room temperature form, suggesting a structural phase transition exists between room temperature and 45 °C. Search-match analysis confirms that no decomposition materials were formed, thereby confirming a phase transition has occurred. The powder pattern was indexed and the peak positions were put through the Crysfire suite of programs using the indexing program Dicvol.⁴⁹⁻⁵¹ The solutions were then evaluated using Chekcell.⁴⁸ Based on these findings a

series of LeBail refinements were completed for the high temperature form of $[\text{In}([\text{15}] \text{crown-5})_2][\text{OTf}]$ using tetragonal, orthorhombic and monoclinic structural models. Refinements completed using the monoclinic and orthorhombic models, in space groups Pm and P222, respectively produced the best agreement with the experimental data (Figure 10). The orthorhombic model in space group P222, with a larger unit cell, produced a superior fit when compared with the other proposed models. A series of LeBail refinements were also completed for the monoclinic model with a larger unit cell. However, no improvement in the goodness-of-fit parameters was observed.

Close inspection of the peaks in the 2θ region $5^\circ - 20^\circ$ demonstrates that the orthorhombic model (P222) with a larger unit cell accurately models the peak splitting at approximately 10° (Figure 11(b)). The high temperature form of $[\text{In}([\text{15}] \text{crown-5})_2][\text{OTf}]$ is therefore believed to be an orthorhombic cell, in space group P222, with a large unit cell ($a = 9.2795(9)$, $b = 9.0136(7)$, $c = 28.587(3)$ and $V = 2391.1(4)$). The tripling of the unit cell in the c dimension is believed to arise from tilting of the $[\text{In}([\text{15}] \text{crown-5})_2]$ complex and/or a redistribution of the triflate species within the unit cell. However, given the quality of the current dataset, as well as the complex nature of the structure and abundance of lighter atoms within the unit cell, it was not possible to fully solve the structure at 45°C .

Theoretical Calculations of ^{115}In EFG and NS tensors

First principles calculations of the indium NMR tensor parameters were performed in order to correlate the tensor parameters and orientations with structure and symmetry, as well as to provide a deeper insight into their origins. The development of such correlations is helpful in modelling the structures of indium-containing systems for which single crystals suitable for XRD

experiments are unobtainable. Due to the periodic nature of most of the systems herein, DFT plane-wave pseudopotential methods implemented in the CASTEP software package were used for the calculation of NMR parameters. The results of these calculations are compared to the experimental values in Table 2.

The calculated C_Q values are overestimated for most cases; however, certain experimental trends are replicated (*vide infra*). Plotting the experimental values of C_Q versus calculated values yields reasonably good linear correlation ($R^2 = 0.934$, Figure 12(a)). In contrast, the correlation for the experimental and calculated η_Q is poorer by comparison ($R^2 = 0.880$, Figure 12(b)); however, this result is not unusual, since the C_Q depends only upon the magnitude of V_{33} , whereas η_Q depends on accurate calculations of all three principal components. As well, there is an excellent correlation between the experimental and calculated isotropic chemical shifts ($R^2(\delta_{\text{iso}}) = 0.999$, shifts converted from the NS scale as described in the caption of Table 2, Figure 13(a)), and good correlations for the spans and skews ($R^2(\Omega) = 0.925$ and $R^2(\kappa) = 0.945$, respectively (Figure 13(b) and 13(c)).

In order to see how the individual components of the ^{115}In EFG and NS tensors are influenced by differences in structure and symmetry, their orientations must be examined in detail. For $[\text{In}][\text{GaCl}_4]$, the largest component of the EFG tensor, V_{33} , is the distinct principal component, and is positioned in the plane containing the four equatorial chlorine atoms, perfectly bisecting the angles $\angle(\text{Cl1-In-Cl2})$ and $\angle(\text{Cl3-In-Cl4})$ (Figure 14(a)), while V_{11} is positioned perpendicular to this plane, and bisects the angles $\angle(\text{Cl1-In-Cl3})$ and $\angle(\text{Cl2-In-Cl4})$. The NS tensor is nearly coincident with the EFG tensor (Table 2), in agreement with experimental predictions.

The orientations of the EFG and NS tensors in InBr and InI are similar, which is unsurprising, since they are isostructural; therefore, we only discuss those of InI (Figure 14(b)). The η_Q value indicates that all three components of the EFG tensor are different. V_{33} is in the mirror plane, oriented exactly along the shortest InI bond. V_{11} and V_{22} bisect the I-In-I angles, with V_{11} in the mirror plane, oriented at 90° from the longest equatorial In-I bonds, and V_{22} in the plane of these bonds. The coordinate axis system of the NS tensor is coincident with that of the EFG tensor, consistent with experimental results.

In the case of [In][OTf], the NMR tensors for both indium sites are very similar. Each indium site has four short In-O contacts from four different OTf groups, which are arranged about a pseudo-twofold rotational axis (though there is no twofold rotational axis at the In site or in the overall cluster model due to the positions of the remaining triflate ligands). V_{33} is oriented close to this pseudo-twofold axis (Figure 14(c)), while V_{11} and V_{22} are oriented in similar environments to one another, resulting in a near zero η_Q value. V_{33} is almost coincident with σ_{33} , as observed experimentally.

In order to reduce computational time and due to positional disorder in the triflate groups, for calculations conducted upon [In([15]crown-5)₂][OTf] the triflate anions were replaced by fluorine atoms (i.e., fluorine atoms were positioned at the Cartesian coordinates of the triflate sulfur atoms). V_{33} , the distinct component, is oriented in the direction perpendicular to the fivefold pseudo-rotational axis, indicating that the largest spatial variations of the electric fields are in this direction (Figure 14(d)). V_{11} and V_{22} are similar in magnitude, with V_{11} aligned close to two of the In-O contacts ($\angle V_{11}\text{-In-O1} = 5.95^\circ$). The NS tensor is oriented such that σ_{33} is near the pseudo-fivefold rotational axis, and nearly perpendicular to V_{33} ($\angle(V_{33}\text{-In-}\sigma_{33}) = 76.06^\circ$), in reasonable agreement with experimental findings. In [In([18]crown-6)][OTf], the EFG tensor

orientation is quite different from that of $[\text{In}([\text{15}]\text{crown-5})_2][\text{OTf}]$, with V_{33} as the unique component oriented in the direction of the sixfold pseudo-rotational axis, close to the shortest In-O distance ($\angle V_{33}\text{-In-O} = 6.05^\circ$) of the trifluoromethanesulfonate group (Figure 14(e)). V_{11} is oriented perpendicular to the shortest In-O contacts ($\angle V_{11}\text{-In-O} = 91.01^\circ$) and nearly aligned with two of the oxygen atoms of the crown ($\angle V_{11}\text{-In-O1} = 7.98$ and $\angle V_{11}\text{-In-O2} = 17.70^\circ$). The largest component of the NS tensor, σ_{33} , is also in the direction of the pseudo-sixfold rotational axis and is nearly coincident with V_{33} .

Finally, a comment is made on the signs of the quadrupolar coupling constants, and the importance of these signs in thinking about the relationships between the tensor parameters, tensor orientations and local In environments. C_Q signs are not available from SSNMR spectra of quadrupolar nuclei, though they are available indirectly from SSNMR spectra of spin-1/2 nuclei which are coupled to quadrupolar nuclei.⁷⁸ However, the signs of C_Q are available from first principles calculations, and do provide some insight into the nature of the environment into which V_{33} is directed. In all of the complexes discussed herein, excepting $[\text{In}([\text{15}]\text{crown-5})_2][\text{OTf}]$, the theoretical C_Q values are negative and the V_{33} components of the EFG tensor are oriented along or near short In-X ($X = \text{Cl}, \text{O}, \text{I}, \text{Br}$) contacts. Interestingly, in $[\text{In}([\text{15}]\text{crown-5})_2][\text{OTf}]$, which has a positive value of C_Q , the V_{33} component is not aligned near any atoms, bonds or other sources of electron density. This is consistent with recent predictions from a detailed theoretical study of the relationships between EFG tensor components, orientation, signs and local structure, in which it is shown that negative electronic charge distributions that are oriented in a particular direction generally produce negative EFGs (i.e., negative values of V_{33}) along this direction, while the absence of such charge distributions results in positive EFGs.⁷⁹

Conclusions

This work represents the first systematic study of low oxidation-state indium complexes using ^{115}In SSNMR. ^{115}In SSNMR is proven to be a valuable tool for characterisation of a variety of low oxidation-state indium complexes. The NMR parameters extracted from the ^{115}In SSNMR spectra provide information about the electronic environment, geometry, symmetry and oxidation states of the indium sites. Such information are particularly useful for systems which are insoluble in most organic solvents (as is the case for most In(I) complexes), and/or systems with unknown structures. The combination of VT ^{115}In SSNMR and pXRD experiments is key in characterising new solid phases; a full examination of dynamical motions on ^{115}In SSNMR spectra is beyond the scope of the current article.

Theoretically calculated ^{115}In EFG and CS tensor parameters are, for the most part, in good correlation with the experimental values. The orientations of the EFG and CS tensor components provide insight into the origin of these tensors and their correlations to molecular structure and symmetry. They can also be helpful, in combination with SSNMR, for proposing structural models in cases where crystallographic data are not available, as in the case of $[\text{In}([18]\text{crown-6})][\text{MCl}_4]$, where $\text{M} = \text{Ga}$ or Al . Finally, ^{115}In SSNMR experiments provide fundamental chemical insights into both older systems that were thought to be well understood and newly synthesised indium complexes which can be useful as either reagents or catalysts used in several types of organic transformations. Aside from being very useful for probing In-containing coordination complexes, ^{115}In SSNMR may find wide use in the study of In-containing materials; in particular, there is much to be learned about the molecular-level structures of InX ($\text{X} = \text{S}, \text{Se}, \text{Te}, \text{etc.}$) nanoparticles and nanowires, In_2O_3 nanocrystals and films, as well as their precursor compounds.⁸⁰⁻⁸⁴ Furthermore, the techniques demonstrated herein

could be readily applied to the study of In-containing metal organic frameworks (MOFs).^{85,86} We hope that this work will encourage the use of ^{115}In SSNMR spectroscopy as a primary technique for probing the indium chemical environments in a wide variety of indium-containing systems.

Acknowledgements

RWS and CLBM thank the Natural Science and Engineering Research Council (NSERC) for supporting this research, and also acknowledge the Ontario Ministry of Research and Innovation for support in the form of Early Researcher Awards. RWS thanks the Canadian Foundation for Innovation (CFI), the Ontario Innovation Trust (OIT), the University of Windsor and NSERC for funding of the solid-state NMR centre at the University of Windsor, and the Center for Catalysis and Materials Research (CCMR) at Windsor for additional support. HH and BFTC thank the Ministry of Training, Colleges and Universities for Ontario Graduate Scholarship and UW for a Tuition Scholarship. Tatjana Milovic and Dr. Kris Harris are thanked for helpful comments and technical assistance. Access to the 900 MHz NMR spectrometer was provided by the National Ultrahigh-Field NMR Facility for Solids (Ottawa, Canada), a national research facility funded by CFI, OIT, Recherche Québec, the National Research Council Canada, and Bruker BioSpin and managed by the University of Ottawa (www.nmr900.ca). NSERC is acknowledged for a Major Resources Support grant. BFTC would like to thank Dr S. Holger Eichhorn for assistance with the variable-temperature powder X-ray diffraction experiments.

Supporting Information Available

Electronic Supplementary Information (ESI) available: additional experimental details and NMR data. See DOI: 10.1039/XXXXXXXXX.

References

1. B. D. Ellis, C. L. B Macdonald, *Coord. Chem. Rev.*, 2007, **251**, 936.
2. P. J. Dyson, *Coord. Chem. Rev.*, 2004, **248**, 2443.
3. D. J. Mindiola, *Acc. Chem. Res.*, 2006, **39**, 813.
4. P. W. Roesky, *Dalton Trans.*, 2009, 1887.
5. C. E. Housecroft, *Compr. Coord. Chem.*, II 2004, **5**, 555.
6. G. Linti, H. Schnockel, *Coord. Chem. Rev.*, 2000, **206**, 285.
7. D. G. Tuck, *Chem. Soc. Rev.*, 1993, **22**, 269.
8. C. L. B Macdonald, B. D. Ellis, In *Encyclopedia of Inorganic Chemistry*; R. B. King, Ed.; John Wiley & Sons Ltd, 2005.
9. C. G. Andrews, C. L. B. Macdonald, *J. Organomet. Chem.*, 2005, **690**, 5090.
10. C. G. Andrews, C. L. B. Macdonald, *Angew. Chem. Int. Ed.*, 2005, **44**, 7453.
11. "The Group 13 Metals Aluminium, Gallium, Indium and Thallium. Chemical Patterns and Peculiarities" (S. Aldridge; A. J. Downs, Eds.) John Wiley & Sons: Chichester, U.K, 2011.
12. S. Aldridge, *Angew. Chem. Int. Ed.*, 2006, **45**, 8097.
13. B. F. T. Cooper, C. L. B. Macdonald, *J. Organomet. Chem.*, 2008, **693**, 1707.
14. R. J. Baker, C. Jones, *Coord. Chem. Rev.*, 2005, **249**, 1857.
15. C. Gemel, T. Steinke, M. Cokoja, A. Kemper, R. A. Fischer, *Eur. J. Inorg. Chem.*, 2004, 4161.
16. U. Schneider, S. Kobayashi, *Acc. Chem. Res.*, 2012, **45**, 1331.
17. J. A. J. Pardoe, A. J. Downs, *Chem. Rev.*, 2007, **107**, 2.

18. B. F. T. Cooper, H. Hamaed, W. W. Friedl, M. R. Stinchcombe, R. W. Schurko, C. L. B. Macdonald, *Chem. Eur. J.*, 2011, **17**, 6148.
19. L. A. Errico, M. Weissmann, M. Renteria, *Los Alamos National Laboratory, Preprint Archive, Nuclear Experiment* 2004, 1-6, arXiv:nucl-ex/0408005.
20. L. A. Errico, M. Renteria, *Phys. Rev. B*, 2006, **73**, 115125/115121.
21. R. K. Harris, E. D. Becker, S. M. Cabral De Menezes, R. Goodfellow, P. Granger, *Pure Appl. Chem.*, 2001, **73**, 1795.
22. F. Chen, G. Ma, G. Cavell, V. V. Terskikh, R. E. Wasylshen, *Chem. Commun.*, 2008, 5933.
23. B. R. McGarvey, C. O. Trudell, D. G. Tuck, L. Victoriano, *Inorg. Chem.*, 1980, **19**, 3436.
24. R. Colton, D. Dakternieks, J. Hauenstein, *Aust. J. Chem.*, 1981, **34**, 949.
25. M. A. Malyarick, A. B. Ilyuhin, S. P. Petrosyants, *Polyhedron* 1993, **12**, 2403.
26. F. Cheng, S. I. Friend, A. L. Hector, W. Levason, G. Reid, M. Webster, W. Zhang, *Inorg. Chem.*, 2008, **47**, 9691.
27. P. Caravan, C. Orvig, *Inorg. Chem.*, 1997, **36**, 236.
28. A. N. Kuznetsov, B. A. Popovkin, W. Henderon, M. J. Taylor, L. Bengtsson-Kloo, *Dalton*, 2000, 1777.
29. N. W. Alcock, I. A. Degnan, O. W. Howarth, M. G. H. Wallbridge, *J. Chem. Soc., Dalton Trans.*, 1992, 2775.
30. J. F. Hinton, R. W. Briggs, *NMR Period. Table*, 1978, 279.
31. M. A. Malyarick, S. P. Petrosyants, *Inorg. Chem.*, 1993, **32**, 2265.

32. J. Kodweiss, D. Kohnlein, G. Kossler, O. Lutz, W. Messner, K. R. Mohn, A. Nolle, G. Nothaft, P. Rupperts, N. Steinhauser, D. Zepf, E. Haid, W. Schich, *Z. Naturforsch., A: Phys. Sci.*, 1986, **41A**, 471.
33. Y. Tomita, K. Yamada, H. Ohki, T. Okuda, *Z. Naturforsch., A: Phys. Sci.*, 1998, **53**, 466.
34. E. V. Schmidt, V. L. Ermakov, O. I. Gnezdilov, V. L. Matukhin, B. V. Korzun, A. A. Fadeeva, I. K. Khabibullina, *J. Appl. Spectrosc.*, 2009, **76**, 667.
35. W.-S. Jung, O. H. Han, S.-A. Chae, *Mater. Lett.*, 2007, **61**, 3413.
36. K. Yamada, K. Kumano, T. Okuda, *Solid State Ionics*, 2005, **176**, 823.
37. K. Yamada, K. Kumano, T. Okuda, *Solid State Ionics*, 2006, **177**, 1691.
38. O. H. Han, H. K. C. Timken, E. Oldfield, *J. Chem. Phys.*, 1988, **89**, 6046.
39. I. K. Khabibullin, V. L. Matukhin, V. L. Ermakov, O. I. Gnezdilov, B. V. Korzun, E. V. Schmidt, *Semiconductors*, 2009, **43**, 1.
40. Y. Tomita, H. Yonekura, Y. Yamauchi, K. Yamada, K. Kobayashi, *Z. Naturforsch., A: Phys. Sci.*, 2002, **57**, 447.
41. F. Chen, G. Ma, G. M. Bernard, R. G. Cavell, R. McDonald, M. J. Ferguson, R. E. Wasylshen, *J. Am. Chem. Soc.*, 2010, **132**, 5479.
42. A. Y. H. Lo, T. Jurca, D. S. Richeson, D. L. Bryce, *J. Phys. Chem. Lett.*, 2010, **1**, 3078.
43. W. Boehlmann, O. Klepel, D. Michel, H. Papp, *Stud. Surf. Sci. Catal.*, 2002, **142B**, 1355.
44. T. Iijima, K. Hashi, A. Goto, T. Shimizu, S. Ohki, *Jpn. J. Appl. Phys., Part 1*, 2006, **45**, 651.
45. S. J. Clark, M. D. Segall, C. J. Pickard, P. J. Hasnip, M. I. J. Probert, K. Refson, M. C. Payne, *Z. Kristallogr.*, 2005, **220**, 567.

46. C. L. B. Macdonald, A. M. Corrente, C. G. Andrews, A. Taylor, B. D. Ellis, *Chem. Commun.*, 2004, 250.
47. A. C. Larson, R. B. V. von Dreele, Los Alamos National Laboratory, Report No. LA-UR-86-748, 1987.
48. W. Kraus, G. Nolze, *J. Appl. Cryst.*, 1996, **29**, 301.
49. R. Shirley, The CRYSFIRE System for Automatic Powder Indexing: v9.46.08, 2004
50. D. Louer, M. Louer, *J. Appl. Cryst.*, 1972, **5**, 271.
51. A. Boultif, D. Louer, *J. Appl. Cryst.*, 1991, **24**, 987.
52. D. Massiot, I. Farnan, N. Gautier, D. Trumeau, A. Trokiner, J. P. Coutures, *Solid State Nucl. Magn. Reson.*, 1995, **4**, 241.
53. A. Medek, V. Frydman, L. Frydman, *J. Phys. Chem. A*, 1999, **103**, 4830.
54. D. Massiot, F. Fayon, M. Capron, I. King, S. Le Calve, B. Alonso, J.-O. Durand, B. Bujoli, Z. Gan, G. Hoatson, *Magn. Reson. Chem.*, 2002, **40**, 70.
55. L. A. O'Dell, R. W. Schurko, *Chem. Phys. Lett.*, 2008, **464**, 97.
56. E. Kupce, R. Freeman, *J. Magn. Reson. Ser. A*, 1995, **115**, 273.
57. K. R. Thurber, R. Tycko, *J. Magn. Reson.*, 2009, **196**, 84.
58. G. Meyer, T. Staffel, *Z. Anorg. Allg. Chem.*, 1989, **574**, 114.
59. G. Meyer, T. Staffel, M. Irmeler, *Thermochim. Acta*, 1990, **160**, 63.
60. T. Staffel, G. Meyer, *Z. Anorg. Allg. Chem.*, 1987, **552**, 113.
61. C. J. Pickard, F. Mauri, *Phys. Rev. B: Condens. Matter Mater. Phys.*, 2001, **63**, 245101/1.
62. J. P. Perdew, K. Burke, M. Ernzerhof, *Phys. Rev. Lett.*, 1996, **77**, 3865.
63. J. P. Perdew, K. Burke, M. Ernzerhof, *Phys. Rev. Lett.*, 1998, **80**, 891.
64. A. Higelin, U. Sachs, S. Keller, I. Krossing, *Chem. Eur. J.*, 2012, **18**, 10029.

65. H. Schmidbaur, A. Schier, *Organometallics*, 2008, **27**, 2361.
66. F. Levy, E. Mooser, *Helv. Phys. Acta*, 1972, **45**, 69.
67. H. Hamaed, M. W. Laschuk, V. V. Terskikh, R. W. Schurko, *J. Am. Chem. Soc.*, 2009, **131**, 8271.
68. A. H. Barrett, M. Mandel, *Phys. Rev.*, 1958, **109**, 1572.
69. R. G. Barnes, P. J. Bray, *J. Chem. Phys.*, 1955, **23**, 407.
70. R. G. Barnes, P. J. Bray, *J. Chem. Phys.*, 1955, **23**, 1178.
71. R. G. Barnes, P. J. Bray, *J. Chem. Phys.*, 1955, **23**, 1177.
72. S. Ogawa, *J. Phys. Soc. Jpn.*, 1958, **13**, 618.
73. T.-C. Wang, *Phys. Rev.*, 1955, **99**, 566.
74. A. H. Reddoch, *J. Chem. Phys.*, 1961, **35**, 1085.
75. G. K. Semin, T. A. Babushkina, G. G. Yohobson, *Nuclear Quadrupole Resonance in Chemistry*; John Wiley & Sons: New York, 1975.
76. L. A. Kloo, M. J. Taylor, *J. Chem. Soc., Dalton Trans.*, 1997, 2693.
77. T. F. Kemp, M. E. Smith, *Solid State Nucl. Magn. Reson.*, 2009, **35**, 243.
78. R. K. Harris, A. C. Olivieri, *Prog. Nucl. Magn. Reson. Spectrosc.*, 1992, **24**, 435.
79. J. Autschbach, S. Zheng, R. W. Schurko, *Conc. Magn. Reson.*, 2010, **36A**, 84.
80. J.-H. Choi, J. J. Oh, Y. Lai, D. K. Kim, T. Zhao, A. T. Fafarman, B. T. Diroll, C. B. Murray, C. R. Kagan, *ACS Nano*, DOI: 10.1021/nn403752d.
81. E. Witt, J. Kolny-Olesiak, *Chem. Eur. J.*, 2013, **19**, 9746.
82. J. C. Shin, D. Y. Kim, A. Lee, H. J. Kim, J. H. Kim, W. J. Choi, H.-S. Kim, K. J. Choi, *J. Cryst. Growth*, 2013, **372**, 15.
83. D. T. Schoen, H. L. Peng, Y. Cui, *ACS Nano*, 2013, **7**, 3205.

84. B. Aleman, J. A. Garcia, P. Fernandez, J. Piqueras, *Superlattices Microstruct.*, 2013, **56**, 1.
85. L. P. Wang, T. Y. Song, C. Li, J. Xia, S. Y. Wang, L. Wang, J. N. Xu, *J. Solid State Chem.*, 2012, **190**, 208.
86. W. B. Ji, H. L. Hu, W. S. Zhang, H. Huang, X. D. He, X. Han, F. F. Zhao, Y. Liu, Z. H. Kang, *Dalton Trans.*, 2013, **42**, 10690.

Scheme 1: The coordination environments of the indium atoms in (a) $[\text{In}][\text{GaCl}_4]$, (b) InI , (c) InBr , (d) $[\text{In}][\text{OTf}]$, (e) $[\text{In}([\text{15}]\text{crown-5})_2][\text{OTf}]$ (OTf = trifluorosulfonato), (f) $[\text{In}([\text{18}]\text{crown-6})][\text{OTf}]$, and (g) the structural model of $[\text{In}([\text{18}]\text{crown-6})[\text{AlCl}_4]$ and $[\text{In}([\text{18}]\text{crown-6})][\text{GaCl}_4]$. The blue bonds in (d) are those within 3 Å of the indium, the solid black bonds are within 3.5 Å and the dashed bonds are within 4 Å.

Figure 1: Experimental (bottom) and simulated (top) ^{115}In SSNMR powder patterns of $[\text{In}][\text{GaCl}_4]$. The MAS spectrum was acquired with $\nu_{\text{rot}} = 18$ kHz, which is fast enough to separate the spinning sidebands from the isotropic powder patterns.

Figure 2: Experimental (bottom) and simulated (top) ^{115}In SSNMR powder patterns of (a) InI and (b) InBr . The MAS spectra were acquired at $\nu_{\text{rot}} = 62.5$ kHz.

Figure 3: Experimental (bottom) and simulated (top) ^{115}In SSNMR powder patterns of $[\text{In}][\text{OTf}]$. The MAS spectrum was acquired at $\nu_{\text{rot}} = 62.5$ kHz. *: Impurity at $-152(100)$ ppm.

Figure 4: Experimental (bottom) and simulated (top) ^{115}In SSNMR powder patterns of $[\text{In}([\text{15}]\text{crown-5})_2][\text{OTf}]$. The MAS spectrum was acquired with $\nu_{\text{rot}} = 12.5$ kHz.

Figure 5: Experimental (bottom) and simulated (top) ^{115}In SSNMR powder patterns of $[\text{In}([\text{18}]\text{crown-6})][\text{OTf}]$. This spectrum was acquired with a short echo delay (8 μs) due to the short $T_2(^{115}\text{In})$.

Figure 6: Experimental (bottom) and simulated (top) ^{115}In SSNMR powder patterns of (a) $[\text{In}([\text{18}]\text{crown-6})][\text{GaCl}_4]$ and (b) $[\text{In}([\text{18}]\text{crown-6})][\text{AlCl}_4]$. The MAS spectra were acquired with $\nu_{\text{rot}} = 50$ kHz, fast enough to separate the spinning sidebands from the isotropic powder patterns. *: Impurity at $-1130(100)$ ppm.

Figure 7: Variable-temperature ^{115}In SSNMR powder patterns of $[\text{In}([\text{15}]\text{crown-5})_2][\text{OTf}]$. The MAS spectra were acquired with $\nu_{\text{rot}} = 12.5$ kHz.

Figure 8: The powder X-ray patterns of $[\text{In}([\text{15}]\text{crown-5})_2][\text{OTf}]$ at (a) room temperature, (b) 45 °C, (c) at room temperature after cooling from 45 °C showing the reversibility of the phase transition and (d) the pattern at 120 °C which shows a complete loss of any crystalline material. The melting point of the sample is between 91-95 °C.

Figure 9: Rietveld refinement of the room temperature pXRD data for $[\text{In}([\text{15}]\text{crown-5})_2][\text{OTf}]$ using the triclinic P-1 model proposed by Cooper *et al.*¹² Refined lattice parameters $a = 8.880(2)$ Å, $b = 9.185(2)$ Å, $c = 9.557(2)$ Å, $\alpha = 102.01(1)^\circ$, $\beta = 91.82(2)^\circ$, $\gamma = 96.85(2)^\circ$, $V = 755.7(3)$ Å³, $wR_p = 5.00$ % and $R_p = 4.02$ %.

Figure 10: LeBail refinements of the pXRD data collected at 45 °C for $[\text{In}([\text{15}]\text{crown-5})_2][\text{OTf}]$ using (a) a monoclinic model in space group Pm with parameters $a = 9.147(3)$ Å, $b = 9.082(4)$ Å, $c = 27.885(9)$ Å, $\beta = 93.86(3)^\circ$, $V = 2311(1)$ Å³, $wR_p = 3.57$ % and $R_p = 2.37$ %, and (b) an orthorhombic model in space group P222 with parameters $a = 9.2795(9)$ Å, $b = 9.0136(7)$ Å, $c = 28.587(3)$ Å, $\beta = 90^\circ$, $V = 2391.1(4)$ Å³, $wR_p = 2.18$ % and $R_p = 1.14$ %.

Figure 11: LeBail refinements of the pXRD data collected at 45 °C for $[\text{In}([\text{15}]\text{crown-5})_2][\text{OTf}]$ between $2\theta = 5^\circ - 20^\circ$ using (a) a monoclinic model in space group Pm with a large unit cell described by a, b, 3c and (b) an orthorhombic model in space group P222 with a large unit cell described by a, b, 3c.

Figure 12: Correlations between the experimental and calculated ^{115}In (a) C_Q and (b) η_Q values. The signs of the experimental C_Q values cannot be determined; thus, only the absolute values of the experimental and theoretical values are plotted.

Figure 13: Correlations between the experimental and calculated ^{115}In (a) isotropic chemical shifts, (b) span (Ω) and (c) skew (κ) values. The κ value of InBr is an outlier compared to all of the other data, and is excluded from the plot.

Figure 14: The ^{115}In EFG tensor orientations in (a) $[\text{In}][\text{GaCl}_4]$, (b) InI (the InBr is the same and thus it is not shown), (c) $[\text{In}][\text{OTf}]$ (In site 2), (d) $[\text{In}([\text{15}]\text{crown-5})_2][\text{OTf}]$, and (e) $[\text{In}([\text{18}]\text{crown-6})][\text{OTf}]$. The blue bonds in (c) are those within 3 Å from the indium, the solid black bonds are within 3.5 Å and the dashed ones are within 4 Å.

Table 1. Summary of the experimental ^{115}In NMR parameters.

	$C_Q(^{115}\text{In})$ (MHz) ^a	η_Q ^b	δ_{iso} (ppm) ^c	Ω (ppm) ^d	κ ^e	α (°) ^f	β (°)	γ (°)
[In][GaCl ₄]	22.0(6)	0.2(1)	-1115(10)	60(20)	0.7(3)	65(20)	8(6)	5(5)
InI	44(1)	0.7(1)	-480(20)	110(50)	0.8(2)	45(40)	5(5)	0
InBr	67(2)	0.58(8)	-580(40)	140(40)	0.4(3)	30(20)	5(5)	30(20)
[In][OTf]	80.5(15)	0.07(3)	-1045(15)	260(60)	0.3(2)	50(30)	3(3)	20(20)
[In([15]crown-5) ₂][OTf]	28.4(10)	0.18(10)	-1192(15)	75(15)	0.2(4)	50(30)	90(10)	5(5)
[In([18]crown-6)][OTf]	108(3)	0.015(15)	-890(50)	380(100)	0.7(2)	-	-	-
[In([18]crown-6)][GaCl ₄]	57.0(15)	0.10(5)	-1110(20)	50(30)	0.2(6)	10(10)	20(10)	10(10)
[In([18]crown-6)][AlCl ₄]	60.2(10)	0.07(6)	-1115(10)	45(30)	0.0(6)	30(20)	35(20)	20(10)

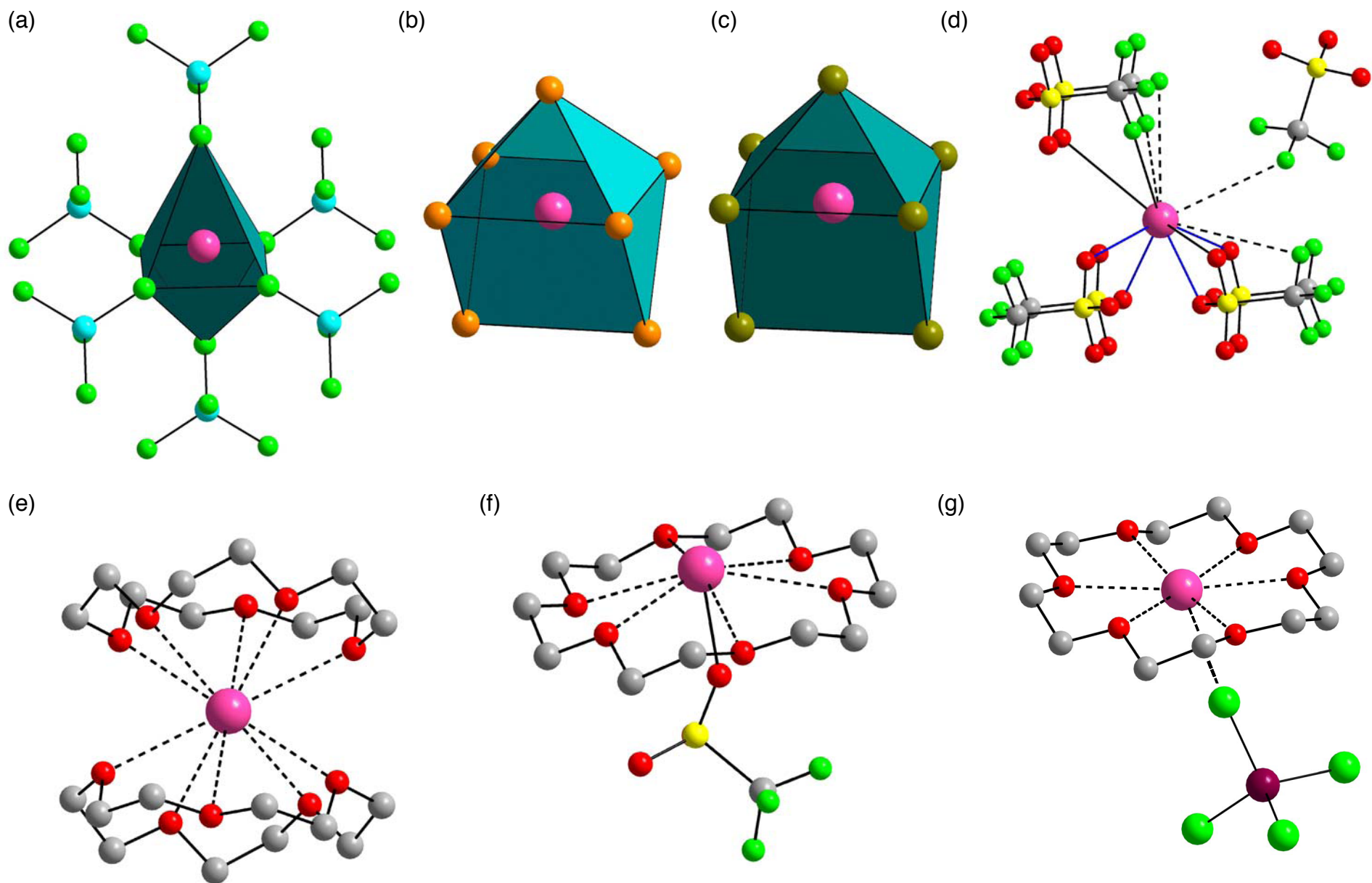
^a $C_Q = eQV_{33}/h$; ^b $\eta_Q = (V_{11} - V_{22})/V_{33}$; ^c $\delta_{\text{iso}} = (\delta_{11} + \delta_{22} + \delta_{33})/3$; ^d $\Omega = \delta_{11} - \delta_{33}$; ^e $\kappa = 3(\delta_{22} - \delta_{\text{iso}})/\Omega$.

^f Conventions for the Euler angles are described in the WSolids software package.

Table 2. Comparison of the experimental and theoretical ^{115}In EFG and CS tensor parameters.

	V_{11} (au)	V_{22} (au)	V_{33} (au)	$C_Q(^{115}\text{In})$ (MHz) ^a	η_Q	δ_{iso} (ppm)	Ω (ppm)	κ	α (°)	β (°)	γ (°)
[In][GaCl ₄] Exp.	-	-	-	22.0(6)	0.2(1)	-1115(10)	60(20)	0.7(3)	65(20)	8(6)	5(5)
[In][GaCl ₄] Cal.	0.1072	0.1094	-0.2166	-39.2	0.02	-1115	112	0.83	90	5	90
InI Exp.	-	-	-	44(1)	0.7(1)	-480(20)	110(50)	0.8(2)	45(40)	5(5)	0
InI Cal.	0.0417	0.1755	-0.2173	-39.3	0.62	-545	334	0.81	0	0	0
InBr Exp.	-	-	-	67(2)	0.58(8)	-580(40)	140(40)	0.4(3)	30(20)	5(5)	30(20)
InBr Cal.	0.0996	0.2982	-0.3978	-72.0	0.50	-583	120	0.94	0	0	0
[In][OTf] Exp.	-	-	-	80.5(15)	0.07(3)	-1045(15)	260(60)	0.3(2)	50(30)	3(3)	30(20)
[In][OTf] Cal. Site 1	0.2106	0.3349	-0.5455	-98.7	0.23	-1083	236	0.44	51	2	22
[In][OTf] Cal. Site 2	0.2484	0.3334	-0.5818	-105.2	0.15	-1075	248	0.56	44	10	28
[In([15]crown-5) ₂][OTf] Exp.	-	-	-	28.4(10)	0.18(10)	-1192(15)	75(15)	0.2(4)	50(30)	90(10)	5(5)
[In([15]crown-5) ₂][OTf] Cal.	-0.0986	-0.1419	0.2405	43.5	0.18	-1153	109	0.30	19	76	13
[In([18]crown-6)][OTf] Exp.	-	-	-	108(3)	0.015(15)	-890(50)	380(100)	0.7(2)	-	-	-
[In([18]crown-6)][OTf] Cal.	0.3131	0.3681	-0.6813	-123.2	0.08	-888	382	0.84	26	4	103

^a Values of C_Q ($C_Q = eQV_{33}/h$) are calculated by converting from atomic units to Hz by multiplying V_{33} by $(eQ/h)(9.7177 \times 10^{-21} \text{ Vm}^{-2})$, where $Q(^{115}\text{In}) = 0.77 \times 10^{-28} \text{ m}^2$. The signs of experimental C_Q values are unknown; signs of theoretically calculated values of C_Q are determined from calculations. ^b The calculated CS are reported with respect to [In][GaCl₄] using the equation: $\delta_{\text{iso}}(\text{sample}) \text{ ppm} = \sigma_{\text{iso}}([\text{In}][\text{GaCl}_4]) \text{ ppm} - \sigma_{\text{iso}}(\text{sample}) \text{ ppm} - 1115 \text{ ppm}$.



Scheme 1. The coordination environments of the indium atoms in (a) $[\text{In}][\text{GaCl}_4]$, (b) InI , (c) InBr , (d) $[\text{In}][\text{OTf}]$, (e) $[\text{In}([\text{15}]\text{crown-5})_2][\text{OTf}]$ (OTf = trifluorosulfonato), (f) $[\text{In}([\text{18}]\text{crown-6})][\text{OTf}]$, and (g) the structural model of $[\text{In}([\text{18}]\text{crown-6})][\text{AlCl}_4]$ and $[\text{In}([\text{18}]\text{crown-6})][\text{GaCl}_4]$. The blue bonds in (d) are those within 3 \AA of the indium, the solid black bonds are within 3.5 \AA and the dashed bonds are within 4 \AA .

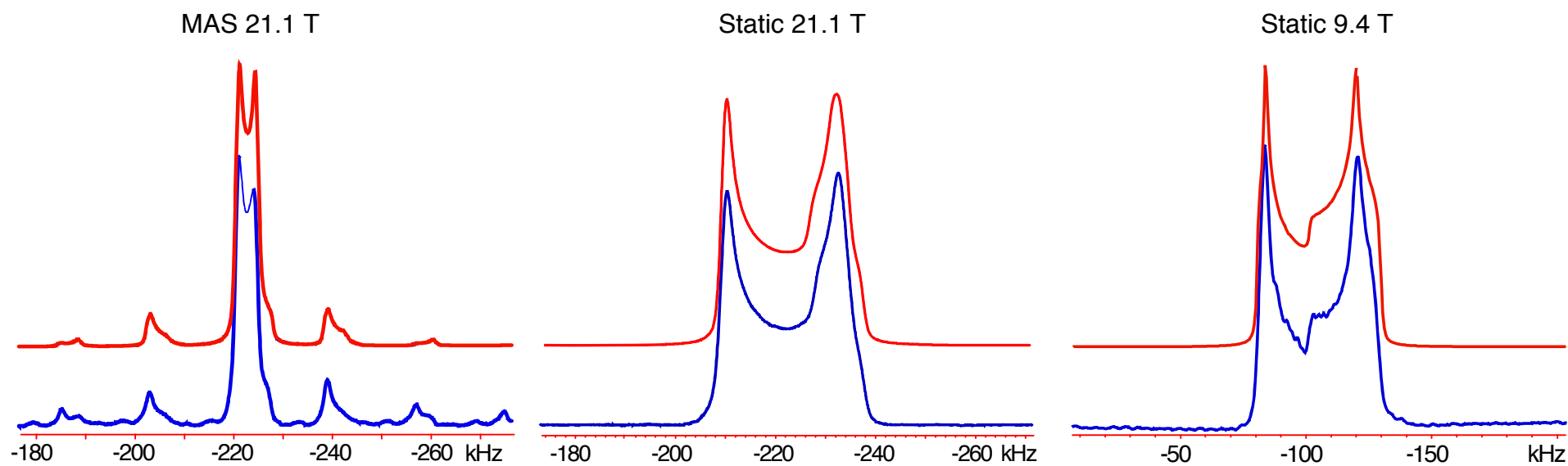


Figure 1. Experimental (bottom) and simulated (top) ^{115}In SSNMR powder patterns of $[\text{In}][\text{GaCl}_4]$. The MAS spectrum was acquired with $\nu_{\text{rot}} = 18$ kHz, which is fast enough to separate the spinning sidebands from the isotropic powder pattern.

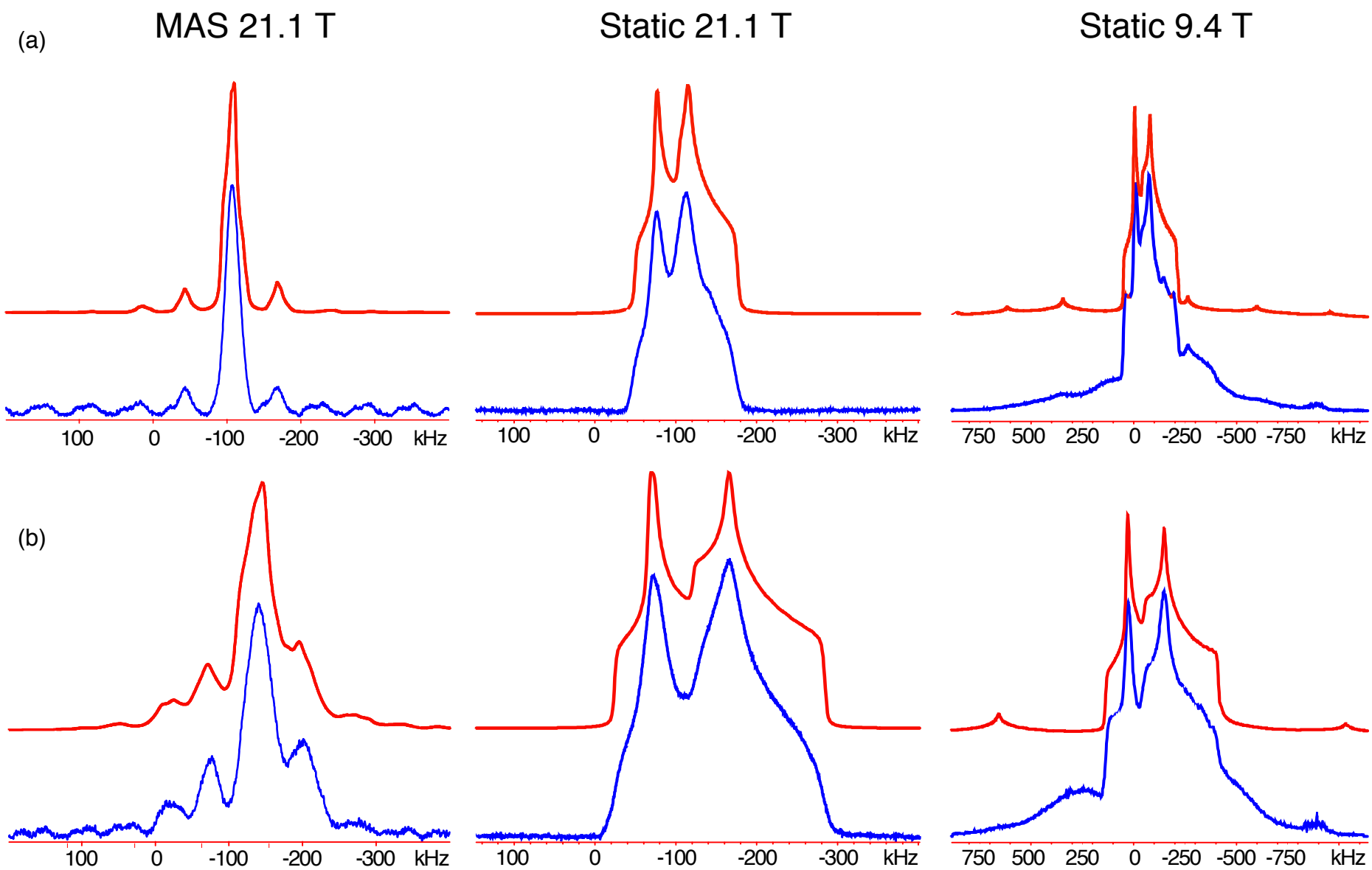


Figure 2. Experimental (bottom) and simulated (top) ^{115}In SSNMR powder patterns of (a) InI and (b) InBr. The MAS spectra were acquired at $\nu_{\text{rot}} = 62.5$ kHz.

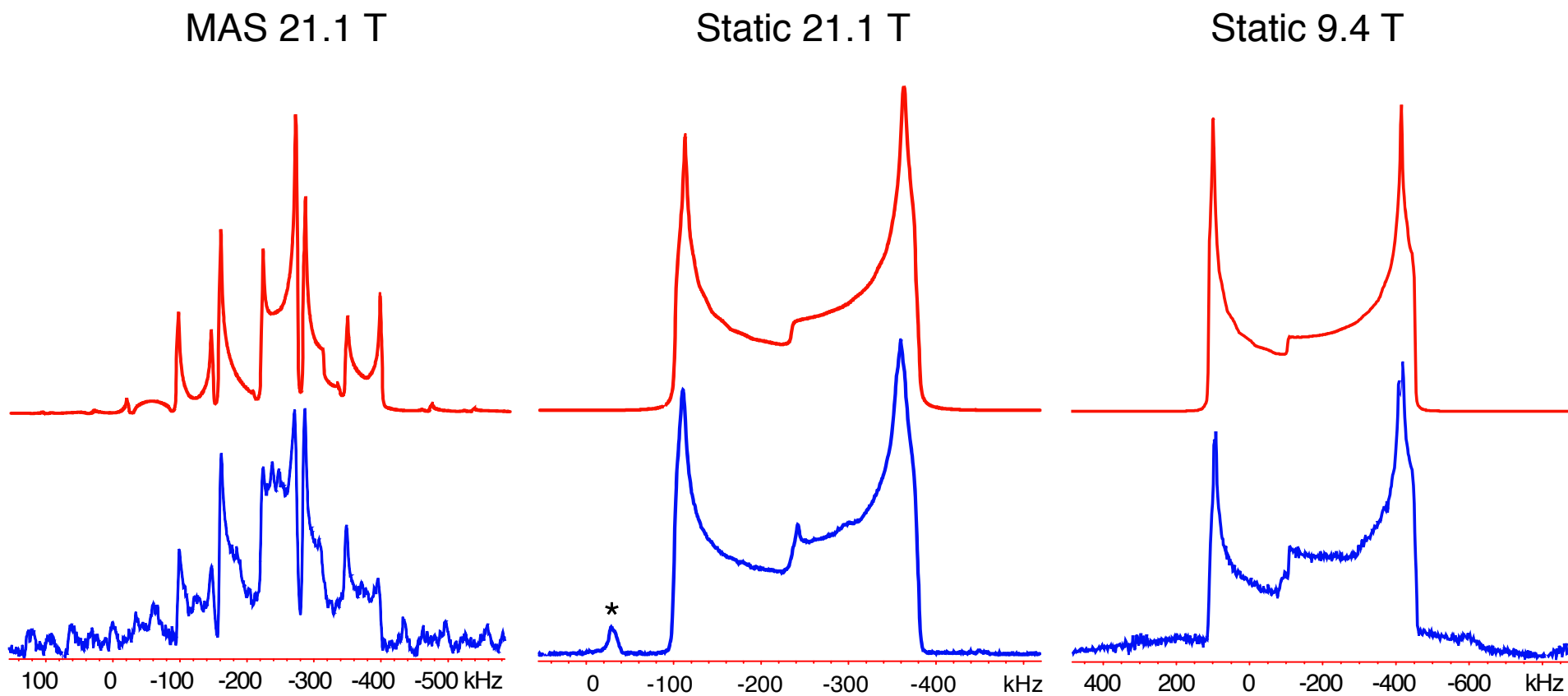


Figure 3. Experimental (bottom) and simulated (top) ^{115}In SSNMR powder patterns of $[\text{In}][\text{OTf}]$. The MAS spectrum was acquired at $\nu_{\text{rot}} = 62.5$ kHz. *: Impurity at $-152(100)$ ppm.

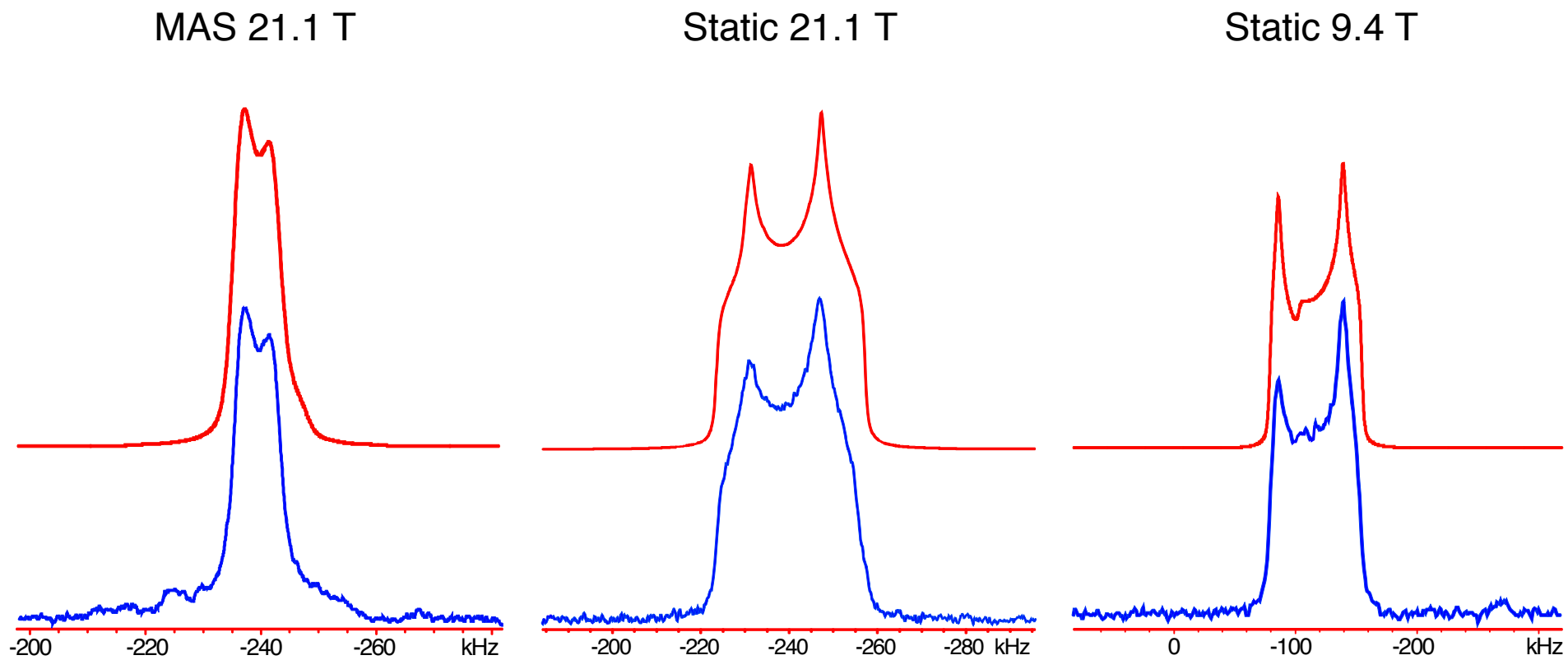


Figure 4. Experimental (bottom) and simulated (top) ^{115}In SSNMR powder patterns of $[\text{In}([15]\text{crown-5})_2][\text{OTf}]$. The MAS spectrum was acquired with $\nu_{\text{rot}} = 12.5$ kHz.

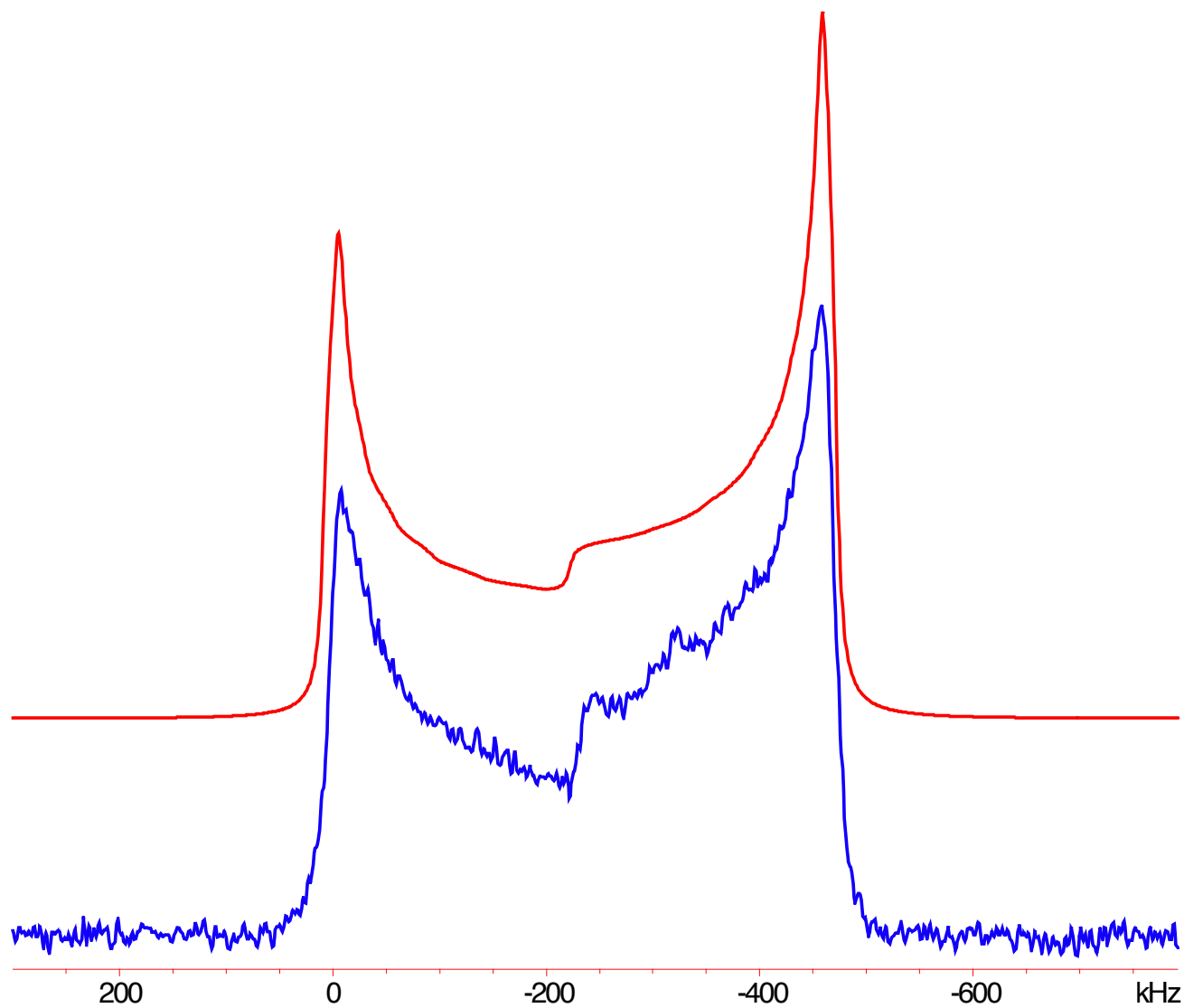


Figure 5. Experimental (bottom) and simulated (top) ^{115}In SSNMR powder patterns of $[\text{In}([\text{18}]\text{crown-6})][\text{OTf}]$. This spectrum was acquired with a short echo delay ($8\ \mu\text{s}$) due to the short $T_2(^{115}\text{In})$.

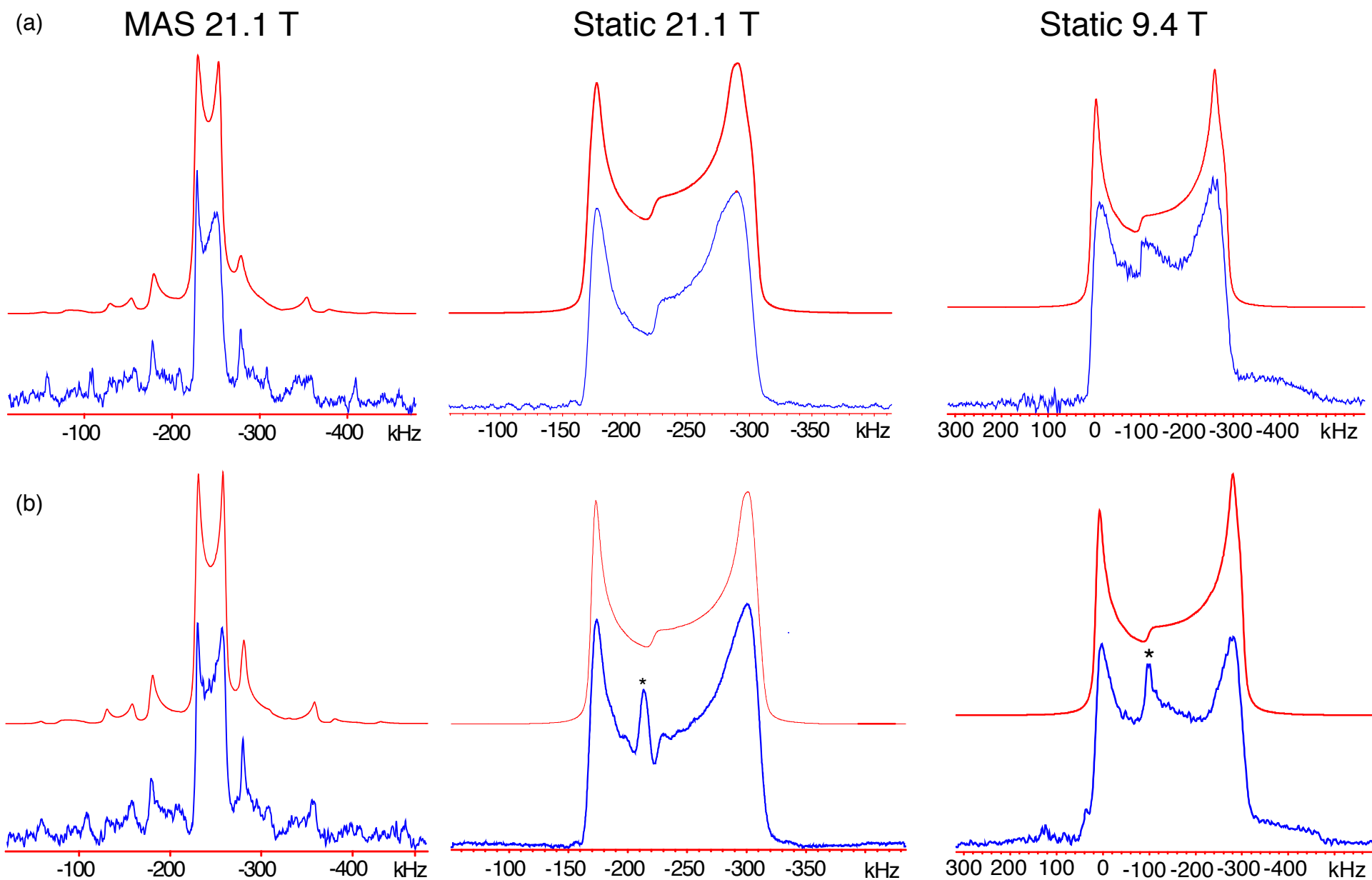


Figure 6. Experimental (bottom) and simulated (top) ^{115}In SSNMR powder patterns of (a) $[\text{In}([\text{18}]\text{crown-6})][\text{GaCl}_4]$ and (b) $[\text{In}([\text{18}]\text{crown-6})][\text{AlCl}_4]$. The MAS spectra were acquired with $\nu_{\text{rot}} = 50$ kHz, fast enough to separate the spinning sidebands from the isotropic powder patterns. *: Impurity at $-1130(100)$ ppm.

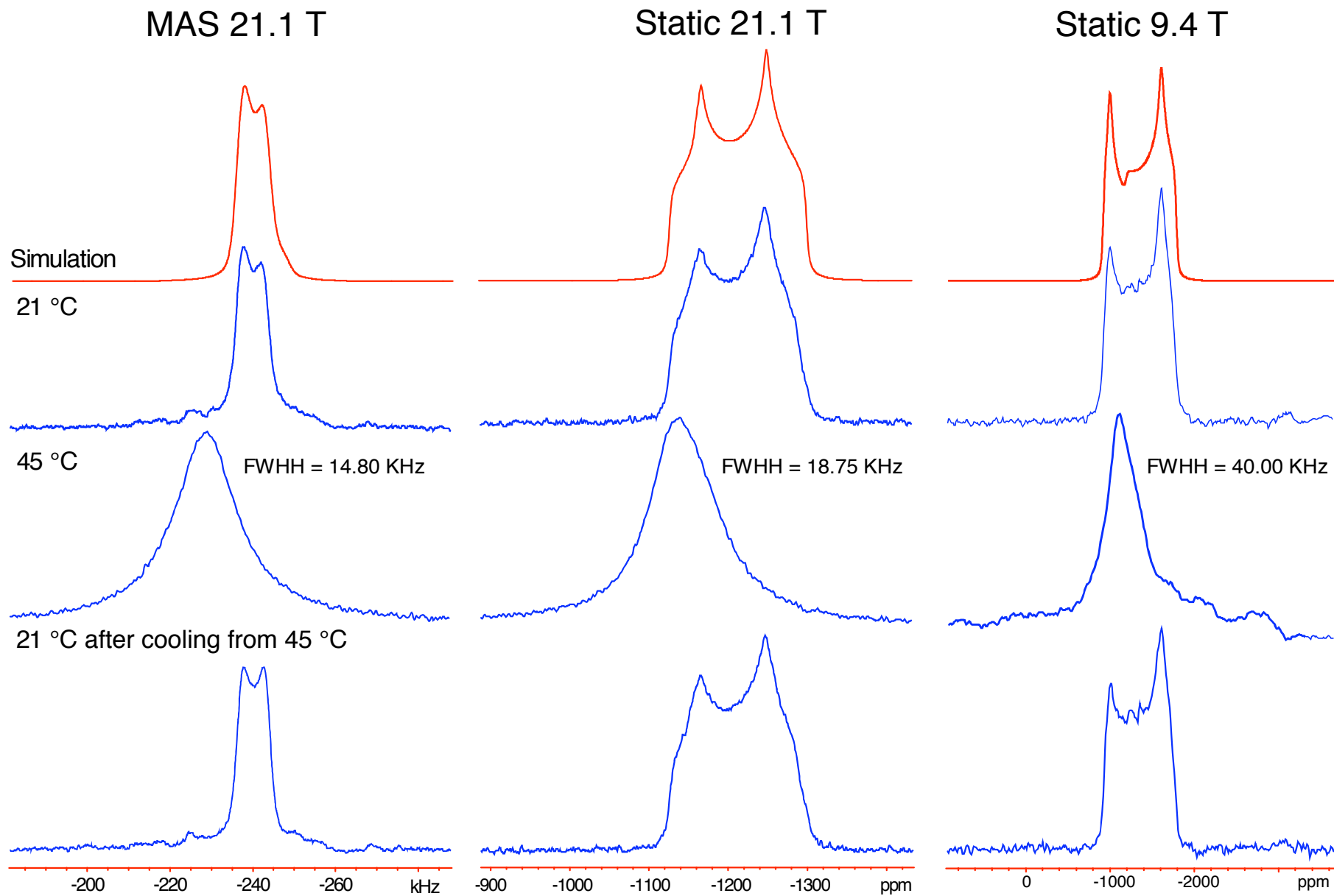


Figure 7. Variable-temperature ^{115}In SSNMR powder patterns of $[\text{In}([\text{15}]\text{crown-5})_2][\text{OTf}]$. The MAS spectra were acquired with $\nu_{\text{rot}} = 12.5$ kHz.

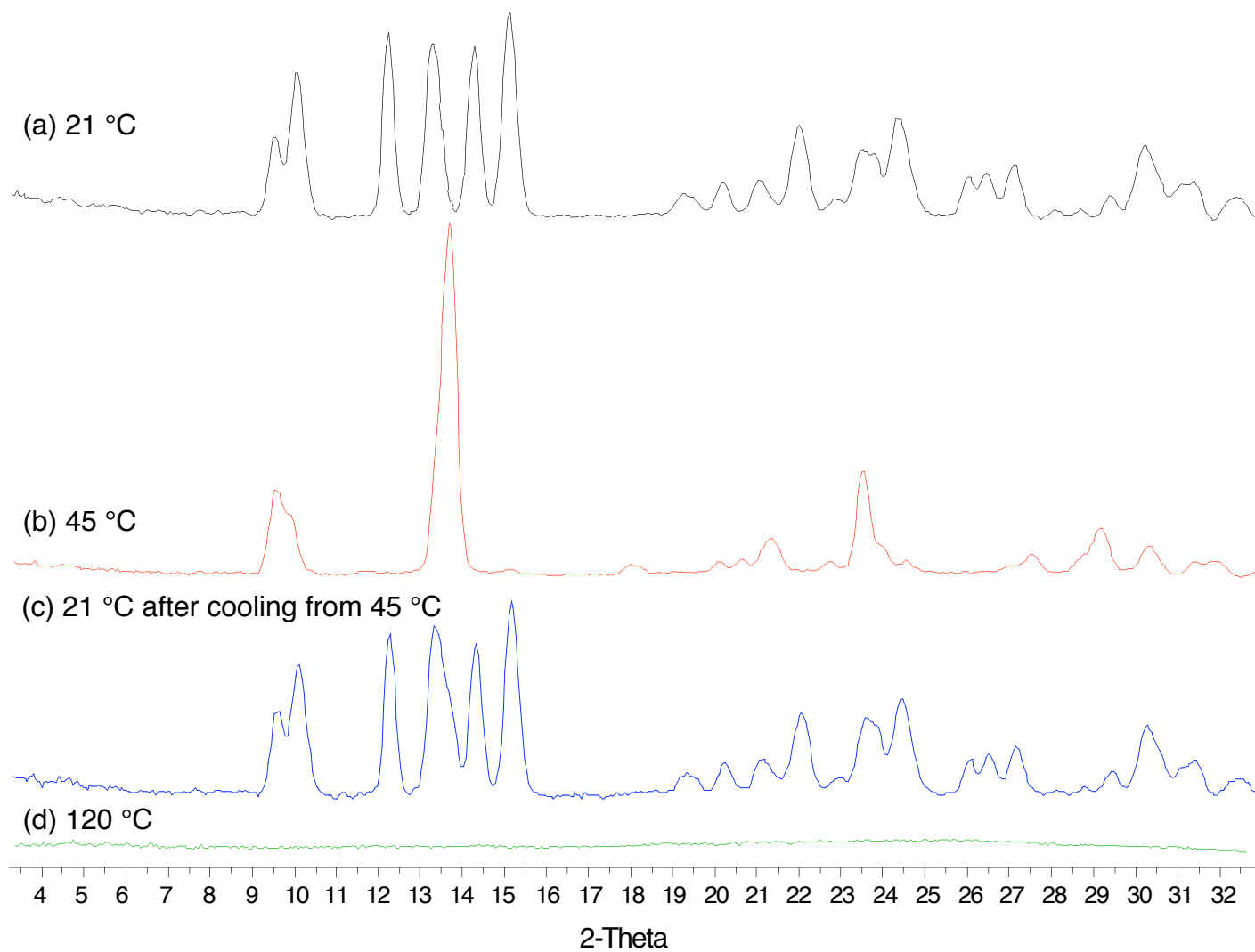


Figure 8. The powder X-ray patterns of $[\text{In}([\text{15}]\text{crown-5})_2][\text{OTf}]$ at (a) room temperature, (b) 45 °C, (c) at room temperature after cooling from 45 °C showing the reversibility of the phase transition and (d) the pattern at 120 °C which shows a complete loss of any crystalline material. The melting point of the sample is between 91-95 °C.

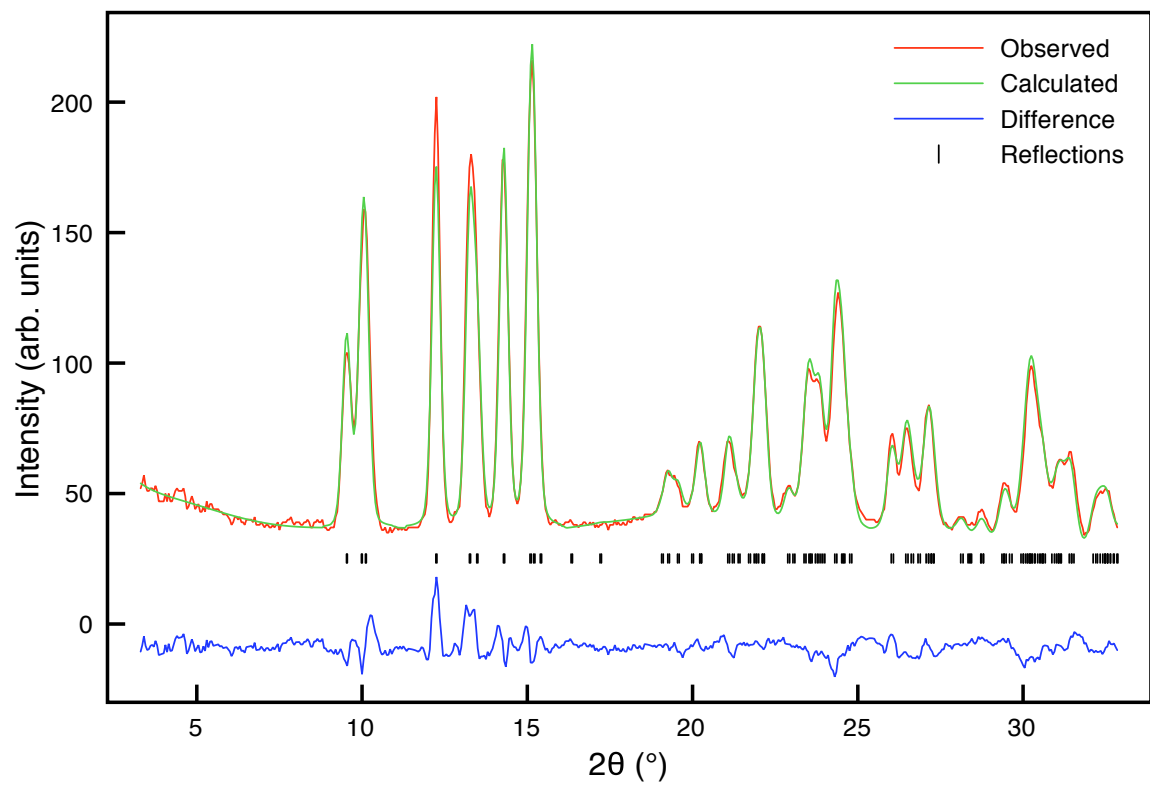


Figure 9. Rietveld refinement of the room temperature pXRD data for $[\text{In}([\text{15}]\text{crown-5})_2][\text{OTf}]$ using the triclinic P-1 model proposed by Cooper *et al.*¹² Refined lattice parameters $a = 8.880(2) \text{ \AA}$, $b = 9.185(2) \text{ \AA}$, $c = 9.557(2) \text{ \AA}$, $\alpha = 102.01(1)^\circ$, $\beta = 91.82(2)^\circ$, $\gamma = 96.85(2)^\circ$ and $V = 755.7(3) \text{ \AA}^3$. $wR_p = 5.00 \%$ and $R_p = 4.02 \%$.

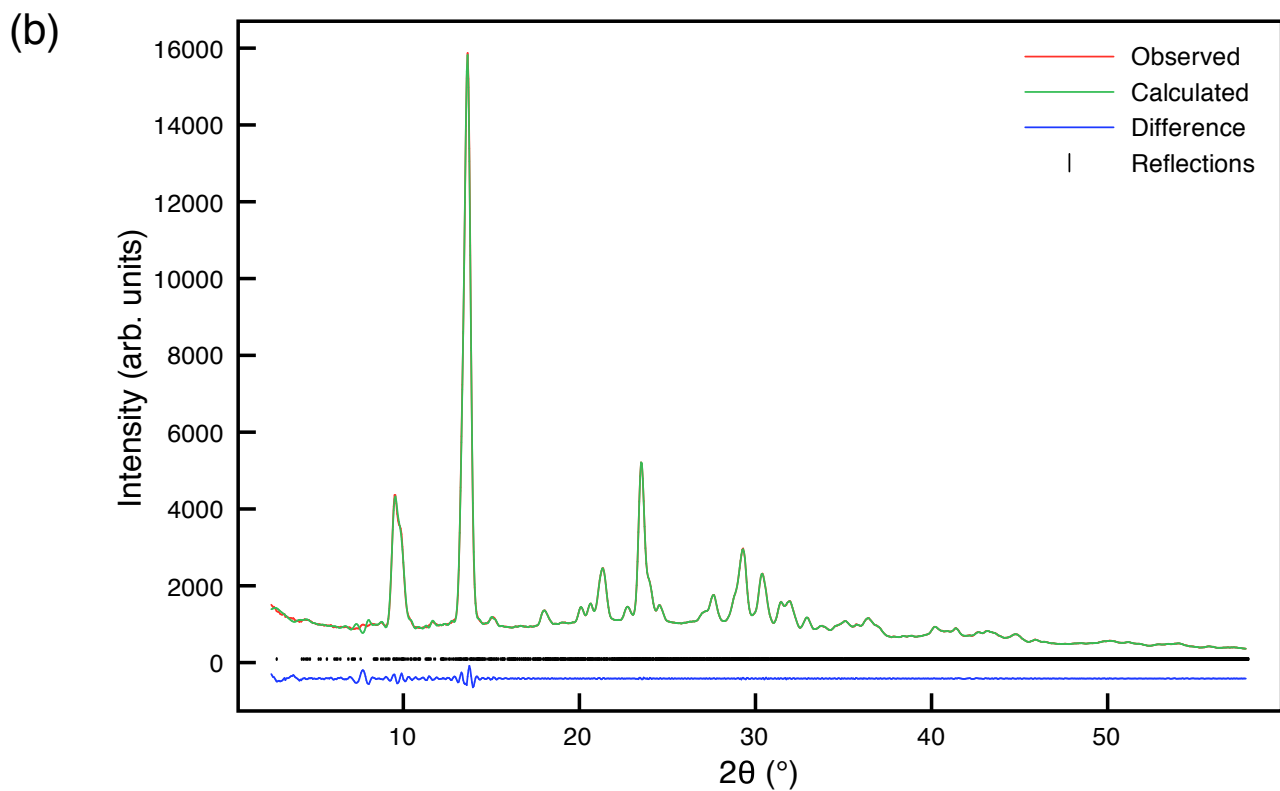
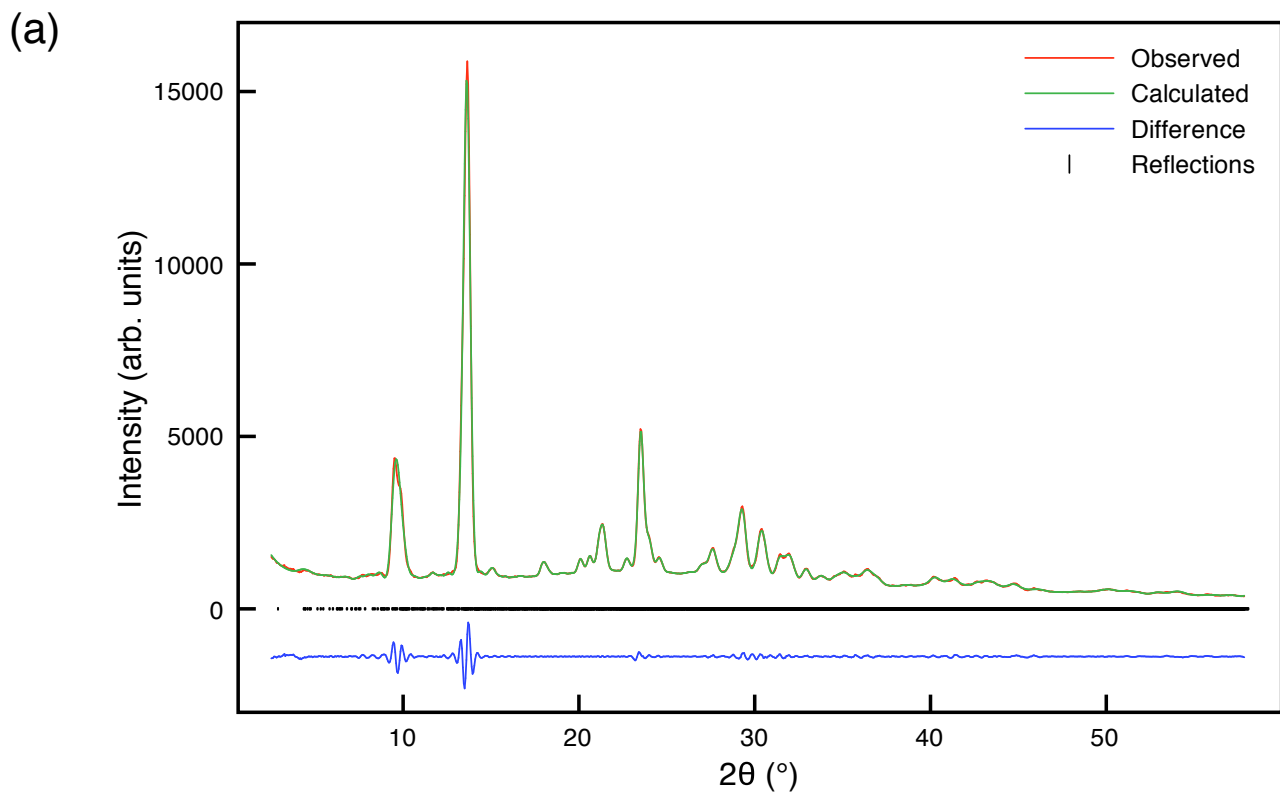


Figure 10. LeBail refinements of the pXRD data collected at 45 °C for $[\text{In}([\text{15}] \text{crown-5})_2][\text{OTf}]$ using (a) a monoclinic model in space group Pm with parameters $a = 9.147(3) \text{ \AA}$, $b = 9.082(4) \text{ \AA}$, $c = 27.885(9) \text{ \AA}$, $\beta = 93.86(3)^\circ$, $V = 2311(1) \text{ \AA}^3$, $wR_p = 3.57\%$ and $R_p = 2.37\%$, and (b) an orthorhombic model in space group P222 with parameters $a = 9.2795(9) \text{ \AA}$, $b = 9.0136(7) \text{ \AA}$, $c = 28.587(3) \text{ \AA}$, $\beta = 90^\circ$, $V = 2391.1(4) \text{ \AA}^3$, $wR_p = 2.18\%$ and $R_p = 1.14\%$.

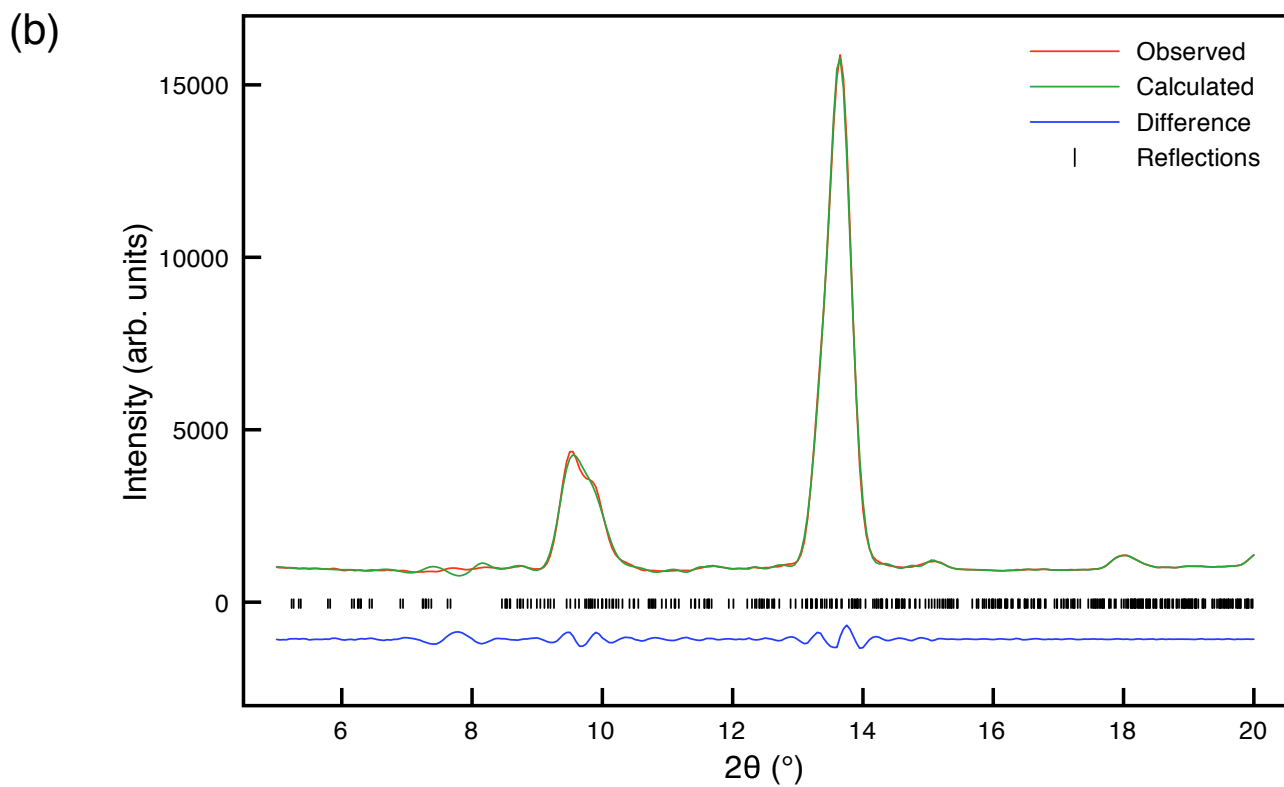
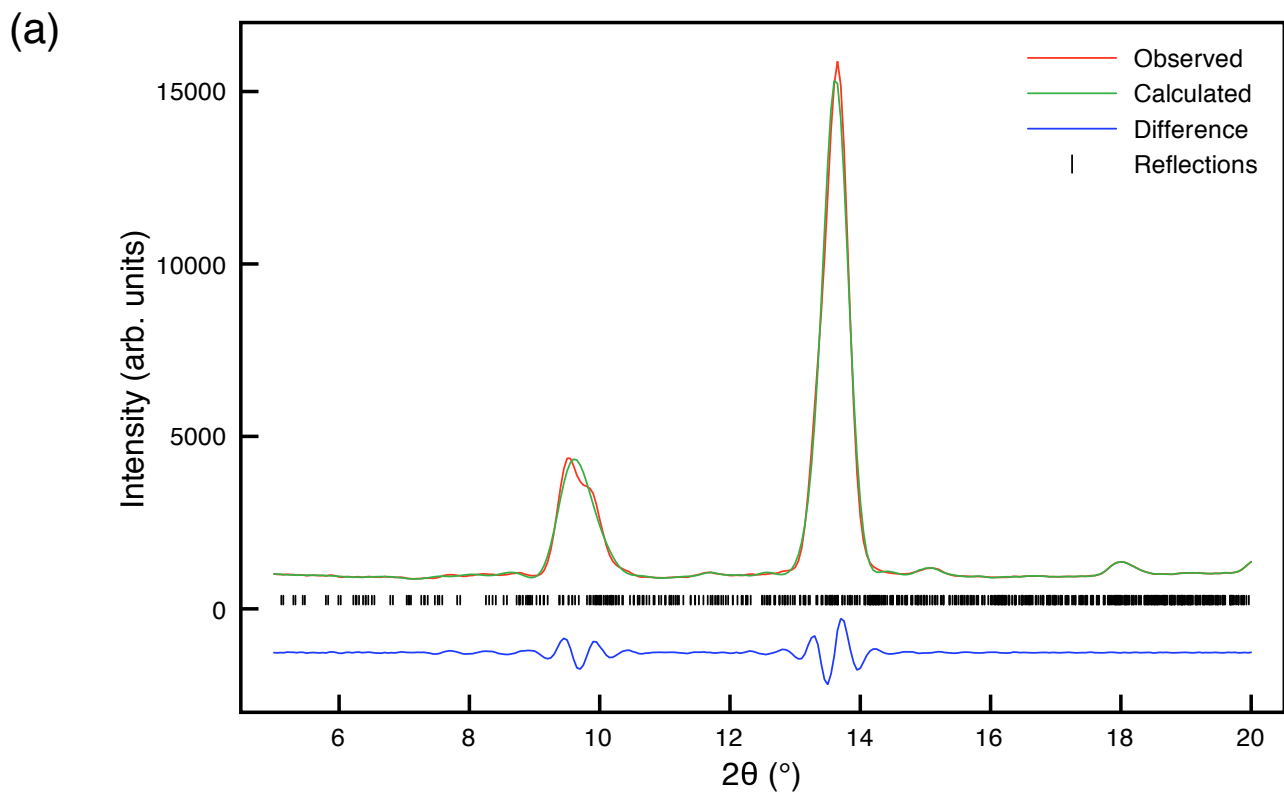
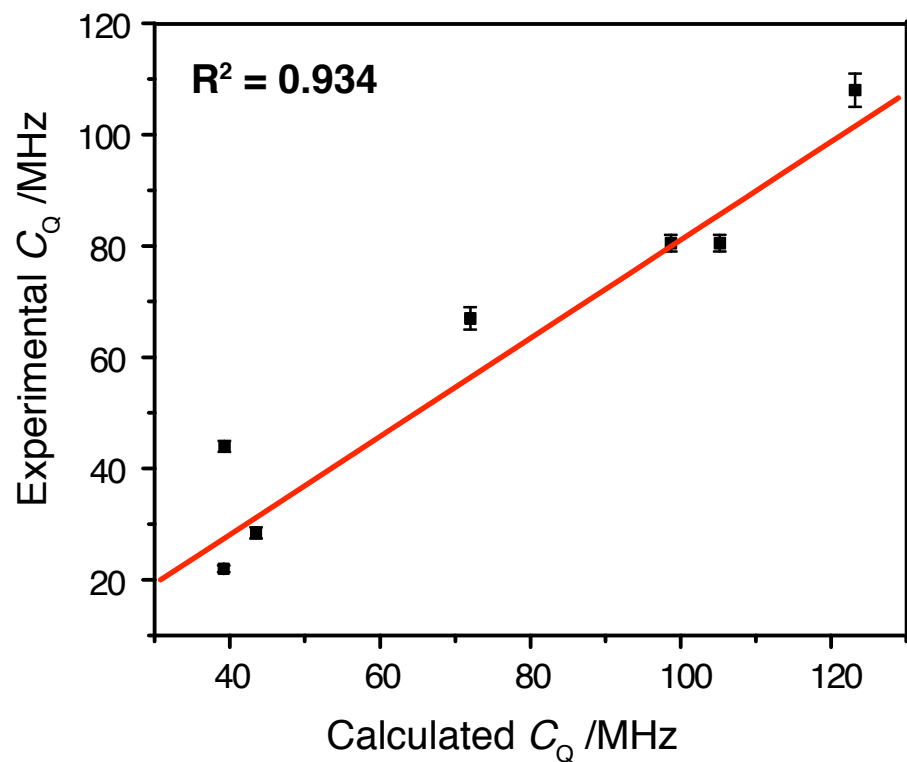


Figure 11. LeBail refinements of the pXRD data collected at 45 °C for $[\text{In}([\text{15}] \text{crown-5})_2][\text{OTf}]$ between $2\theta = 5^\circ - 20^\circ$ using (a) a monoclinic model in space group Pm with a large unit cell described by $a, b, 3c$ and (b) an orthorhombic model in space group P222 with a large unit cell described by $a, b, 3c$.

(a)



(b)

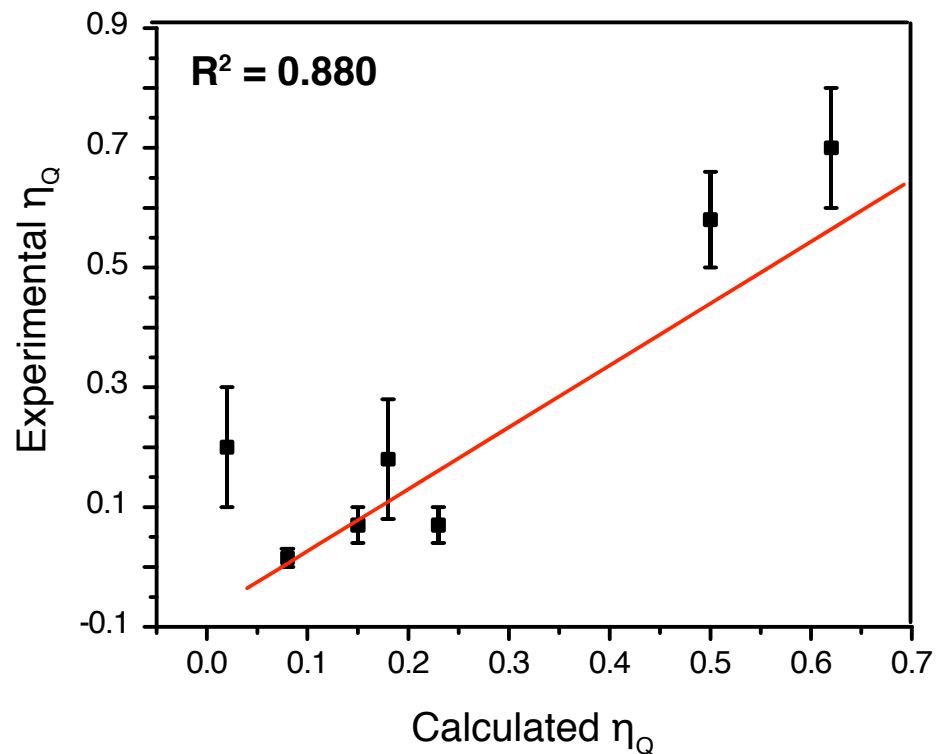


Figure 12. Correlations between the experimental and calculated ^{115}In (a) C_Q and (b) η_Q values. The signs of the experimental C_Q values cannot be determined; thus, only the absolute values of the experimental and theoretical values are plotted.

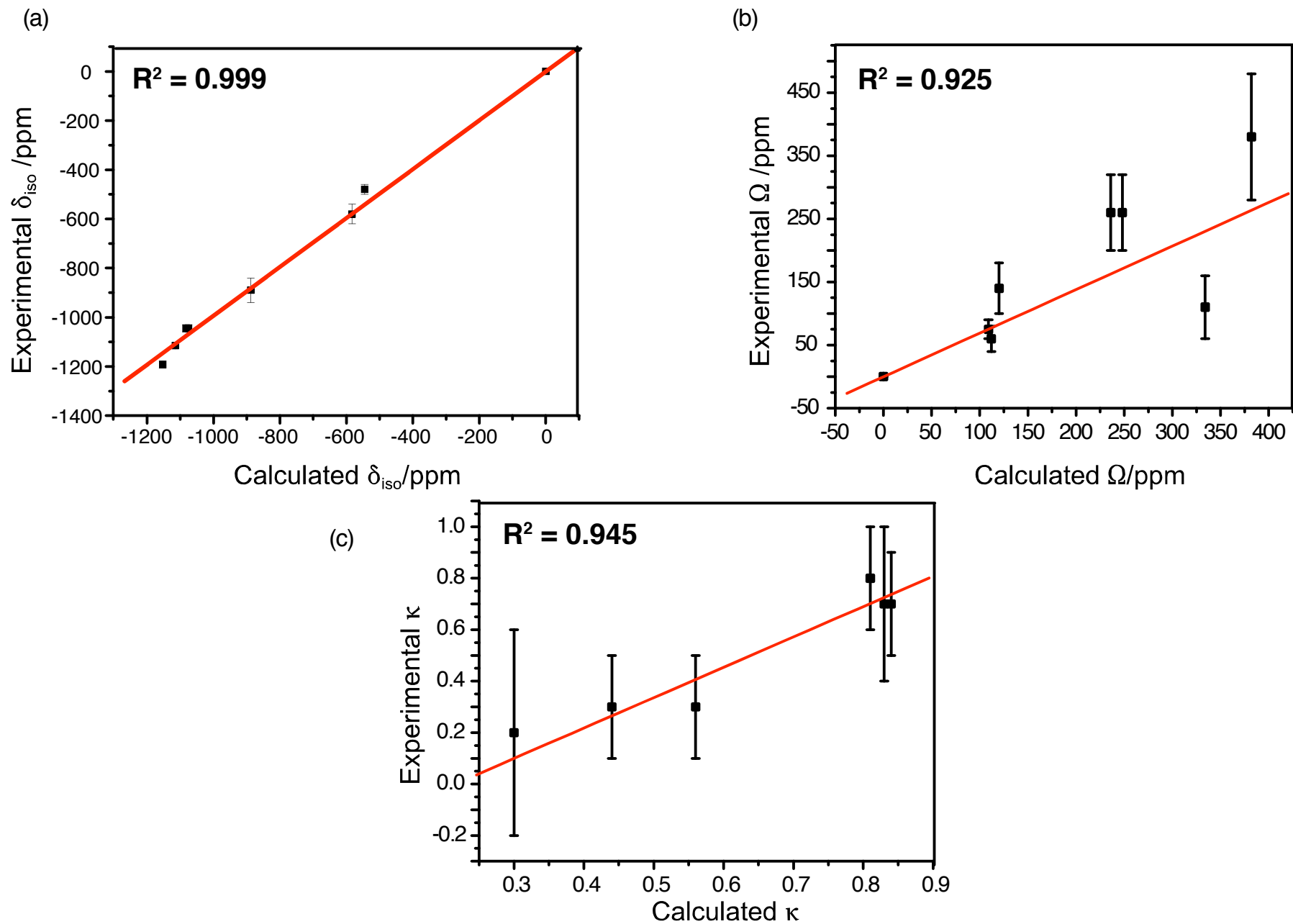


Figure 13. Correlations between the experimental and calculated ^{115}In (a) isotropic chemical shifts, (b) span (Ω) and (c) skew (κ) values. The κ value of InBr is an outlier compared to all of the other data, and is excluded from the plot.

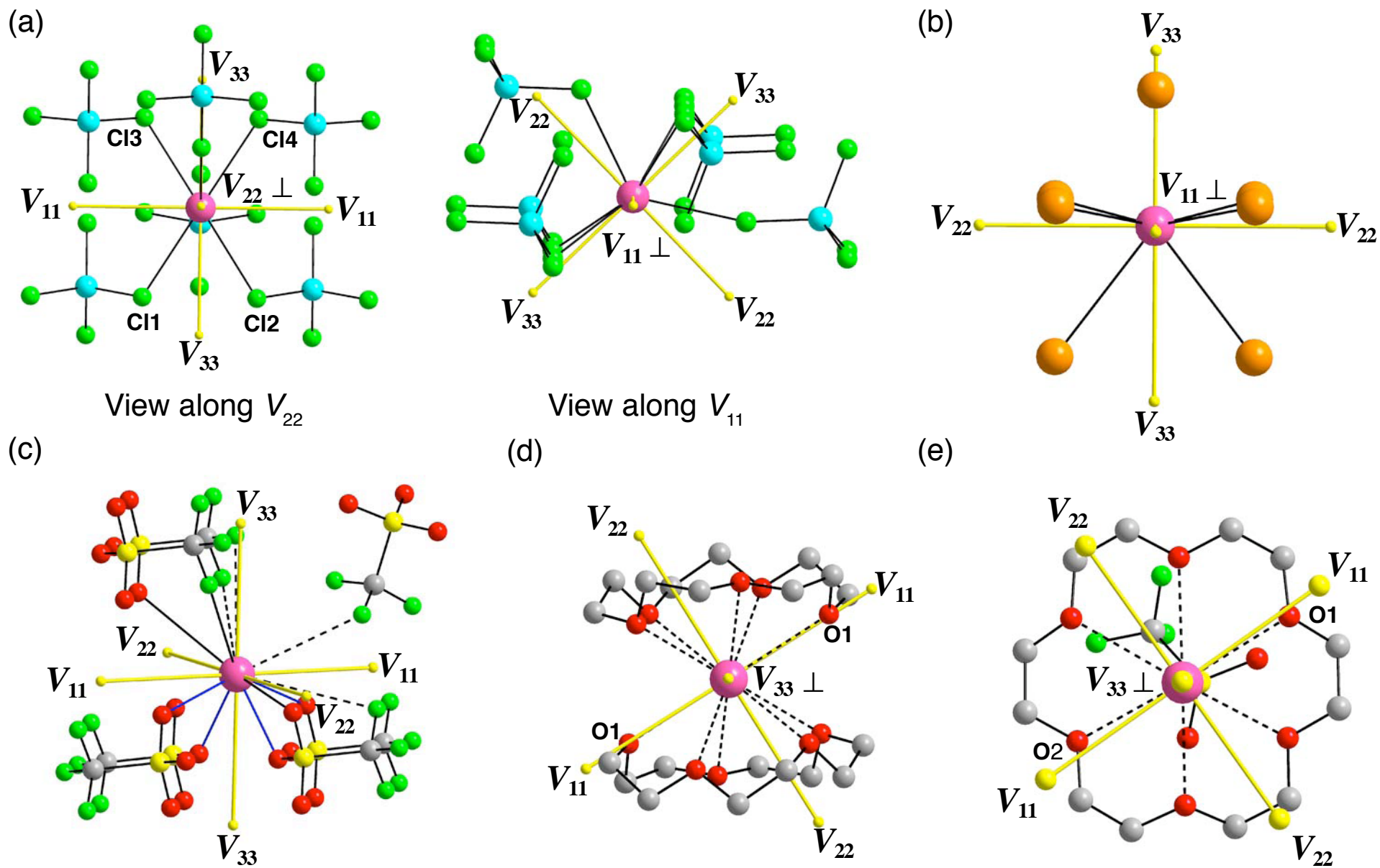


Figure 14. The ^{115}In EFG tensor orientations in (a) $[\text{In}][\text{GaCl}_4]$, (b) InI (the InBr is the same and thus is not shown), (c) $[\text{In}][\text{OTf}]$ (In site 2), (d) $[\text{In}([\text{15}]\text{crown-5})_2][\text{OTf}]$, and (e) $[\text{In}([\text{18}]\text{crown-6})][\text{OTf}]$. The blue bonds in (c) are those within 3 Å from the indium, the solid black bonds are within 3.5 Å and the dashed ones are within 4 Å.